PNAS
www.pnas.org

Supplementary Information for

Phosphate graphene as an intrinsically osteoinductive scaffold for stem cell driven bone regeneration

Anne M. Arnold[a], Brian D. Holt[a], Leila Daneshmandi[b,c,d,e], Cato T. Laurencin[b,c,d,e,f,g], Stefanie A. Sydlik[a,h]

[a]Department of Chemistry, Carnegie Mellon University, Pittsburgh, PA 15213, USA
[b]Connecticut Convergence Institute for Translation in Regenerative Engineering, UConn Health, Farmington, CT 06030, USA
[c]Raymond and Beverly Sackler Center for Biological, Physical and Engineering Sciences, UConn Health, Farmington, CT 06030, USA
[d]Department of Biomedical Engineering, University of Connecticut, Storrs, CT 06269, USA
[e]Department of Orthopaedic Surgery, UConn Health, Farmington, CT 06030, USA
[f]Department of Material Science and Engineering, University of Connecticut, Storrs, CT 06269, USA
[g]Department of Chemical and Biomolecular Engineering, University of Connecticut, Storrs, CT 06269, USA
[h]Department of Biomedical Engineering, Carnegie Mellon University, Pittsburgh, PA 15213, USA

Stefanie A. Sydlik; Cato T. Laurencin
Email: ssydlik@andrew.cmu.edu; laurencin@uchc.edu

www.pnas.org/cgi/doi/10.1073/pnas.1815434116

This PDF file includes:

Supplementary Methods:

GO Preparation. GO was synthesized from graphite using a modified Hummers' method (1) as we have previously reported (2). The reaction was run using 10 g of graphite flakes (graphite flake, natural, –325 mesh, 99.8% metal basis; Alfa Aesar, Ward Hill, MA, USA) that was added to a 2 L flask containing 250 mL of concentrated sulfuric acid (Fisher Scientific, Pittsburgh, PA, USA) cooled over ice while stirring. Then, 20 g of $KMnO_4$ (Sigma–Aldrich, St. Louis, MO, USA) was slowly added over 20–30 min. The reaction was warmed to room temperature and stirred for 2 h followed by gentle heating to 35 °C and stirring for an additional 2 h. The heat was then removed, and the reaction was quenched by slowly adding 1400 mL of deionized (DI) water followed by the slow addition of 20 mL of 30% H_2O_2 (Fisher Scientific). Lastly, 450 mL of DI water was added, and the reaction stirred overnight.

To purify the GO, the reaction mixture was centrifuged at 3,600×*g* for 5 min. The pellet was collected and loaded into 3500 molecular weight cutoff dialysis tubing (SnakeSkin™ dialysis tubing; Thermo Scientific, Waltham, MA, USA) and dialyzed against DI water for 3–7 days. The DI water was changed 2 times the first day and then once a day until the water was clear. Following dialysis, the GO was frozen at –80 °C and lyophilized for 3–5 days to dryness.

PG Synthesis. PG was prepared using an enhanced synthetic procedure over what was previously reported (3) by including a Lewis acid catalyst (magnesium bromide diethyl etherate) to facilitate the reaction. That is, 500 mg of GO, 500 mL of triethyl phosphite (Sigma Aldrich, St. Louis, MO, USA), and 500 mg of magnesium bromide diethyl etherate (Alfa Aesar, Haverhill, MA, USA) were loaded into a flame dried round bottom flask under N_2. The reaction mixture was sonicated (240 W, 42 kHz, ultrasonic cleaner, Kendal) for 1 h followed by the addition of the appropriate anhydrous metal bromide salt: 2.5 g of calcium bromide (Alfa Aesar, Haverhill, MA, USA); 2.5 g of potassium bromide (Alfa Aesar, Haverhill, MA, USA); 2.5 g of lithium bromide (Oakwood Chemicals, Estill, SC, USA); 12.5 g of magnesium bromide (Alfa Aesar, Haverhill, MA, USA); or 2.5 g of sodium bromide (Alfa Aesar, Haverhill, MA, USA). The reaction mixture was sonicated for an additional 30 min and then refluxed at 156 °C under N_2 with stirring for 72 h.

The PG materials were purified by vacuum filtering the reaction, collecting the filter puck, and discarding the filtrate. The resulting product was washed with acetone, centrifuged at 3,600×g for 5 min, and the supernatant discarded. The pellet was re–dispersed in fresh solvent for additional wash steps: once more with acetone, once with ethanol, once with DI water, and an additional 2 washes with acetone. The resulting pellet was dried under vacuum for 24–48 h until dry.

Fourier Transform Infrared Spectroscopy (FTIR) Spectroscopy. A Perkin Elmer Frontier FT–IR Spectrometer with an attenuated total reflectance attachment containing a germanium crystal was used to perform FTIR spectroscopy. Raw spectra were obtained over a range of 4000–700 cm^{-1} with 4 cm^{-1} resolution. All spectra were converted from percent transmittance to absorbance and normalized via the hydroxyl stretch at ~3420 cm^{-1} to an absorbance of 0.1, converted back to percent transmittance, and then offset for clarity. Deconvolution of FTIR spectra from 1900–700 cm^{-1} was conducted with PeakFit (Systat Software Inc.) using the second derivative procedure. Deconvolution parameters used mixed Gaussian–Lorentzian peak shapes and parameter restrictions on the peak center, amplitude, and full width at half maximum of 1, 25, and 50%, respectively.

X–ray Photoelectron Spectroscopy (XPS). XPS was performed on an ESCALAB 250 Xi XPS. Samples were prepared by adhering powders on double sided copper tape. All sample acquisition was conducted using a 200 μm spot size with charge compensation. Elemental scans were obtained in triplicate from 3 separate spots on the material using 5 scans. Quantification of elemental composition was determined using CasaXPS software with a Shirley background using C1s, O1s, P2p, Ca2p, K2s, Li1s, Mg2p, and Na1s peaks for carbon, oxygen, phosphorus, calcium, potassium, lithium, magnesium, and sodium, respectively. High resolution P2p spectra were collected using 10 scans. Raw P2p spectra were smoothed in OriginPro (OriginLab) via the Savitzky–Golay method using a second–degree polynomial every 25 points. Smoothed P2p spectra were Shirley baseline subtracted using Fityk (Version 0.9.8). High resolution C1s spectra were also collected using 10 scans in triplicate for GO and CaPG powders from three separate spots on the materials to apply a relative standard deviation to quantified peak deconvolution data. Raw C1s spectra were smoothed in OriginPro with the Savitzky–Golay method using a second–degree polynomial every 15 points and charge corrected to adventitious carbon at 284.8 eV. The C1s spectra for all materials were then processed using Fityk with Shirley background removal and deconvoluted using Gaussian peak fitting with a full width at half maximum of 1.4 eV. PG C1s spectra peak locations were constrained to ±0.2 eV based on the GO starting material.

Graphenic Pellet Processing. All graphenic powders were dried for 24 h under high vacuum prior to material processing. A custom stainless–steel mold, with an inner diameter of 3.75 mm, was heated to 200 °C in a Fischer Isotemp vacuum oven. The mold was removed from the oven and approximately 20–25 mg of powder was immediately added. The powder was pressed for 1 min on a Columbian D63 1/2 bench vise and then removed from the mold. The PG pellets were then heat treated at 200 °C for 20 min. GO constructs were not subjected to heat treatment since it destroyed the structural integrity of the pellets. All pellets had an average diameter–to–thickness ratio of 3.

Thermogravimetric Analysis (TGA). A PerkinElmer TGA 4000 was used to perform TGA under N_2 from 50–800 °C with a ramp rate of 10 °C min^{-1}. The raw data was analyzed using TRIOS software (TA Instruments).

Raman Spectroscopy. An XploRA ONE™ Raman microscope (HORIBA Scientific) with a 50× objective and 532 nm (2.33 eV) laser line was used to acquire Raman spectra of graphenic powders and pellets. Data was acquired over a range of 63–3624 cm^{-1} (533.8–659.1 nm) with an average step size of 0.125 nm. Peak fitting was performed in MATLAB® (The MathWorks, Inc.). Each spectra was normalized to its maximum; fit with Lorentzian curves for the D, G, D', the peak at ~2450 cm^{-1}, $(G')_1$, $(G')_2$, D+D', and 2G; and fit with a linear combination of a power and linear baseline.

X–ray Powder Diffraction (XRD). XRD was measured on a Rigaku Miniflex XRD over a range of 2.025–49.975 2θ with a step size of 0.050 2θ. Spectra were boxcar smoothed with a window of 5, feature scaled, and offset for clarity.

Compressive Universal Testing. Data was acquired on an Instron 4469 with a load cell of 50 kN. Testing was carried out using strain rates of 0.001, 0.01, and 0.1 s^{-1} at room temperature until

construct failure. Raw data was analyzed and corrected for instrument artifacts according to ASTM D695 (4) using Trios software. Stress–strain curves were truncated at the ultimate stress point to eliminate artifacts from the universal testing geometries. Young's moduli (E) were determined at the onset of the linear region of the stress–strain curve. Toughness (U_T) of graphenic constructs were calculated from the area under the stress–strain curve up to the ultimate stress point.

Dynamic Mechanical Analysis (DMA). DMA was measured on a Discovery Hybrid Rheometer (TA Instruments, New Castle, DE). Compressive DMA testing and torsional shear were performed at room temperature by applying a 0.1% strain at 1 Hz with a 1 N pre–force.

***In vitro* DMA of 3–D Constructs in PBS.** PG pellets were submerged in 0.5 mL of 1× phosphate buffered saline (PBS) in 48–well cell culture plates. Compressive DMA was performed using a sandblasted 8 mm geometry by applying a 0.1% strain at 1 Hz with a 1 N pre–force. Zero–time points were measured immediately after pellets were submerged in PBS equilibrated to 37 °C. Samples were stored at 37 °C for the duration of the experiment, and to maintain volume, DI water was added as needed. After the experiment, intact pellets were frozen at –80 °C and lyophilized until dry for further analysis.

***In vitro* Calcium Elution Study.**

Experimental Design: GO pellets and CaPG pellets were submerged in 1 mL of 1× PBS in 15 mL centrifuge tubes. PBS negative controls were run in parallel. All samples were run with an $n = 3$ sample size and stored at 37 °C for the duration of the experiment (28 days). Zero–time points were measured immediately after pellets were submerged in PBS equilibrated to 37 °C. All time points were obtained by aliquoting 20 μL of sample. Calcium quantification was determined using an *o*–cresolphthalein complexone assay.

***o*–Cresolphthalein Complexone Assay:** Reagent 1 contained 0.3 mol L^{-1} of 2–amino–2–methyl–1–propanol (Alfa Aesar, Haverhill, MA, USA) and adjusted to pH 10.5; Reagent 2 consisted of 0.16 mmol L^{-1} of *o*–cresolphthalein complexone (Alfa Aesar, Haverhill, MA, USA) and 7.0 mmol L^{-1} of 8–hydroxyquinoline (Alfa Aesar, Haverhill, MA, USA). Reagent 1 (145 μL), Reagent 2 (145 μL), and sample of interest (2.9 μL) were added to 96 well cell culture plates and incubated at room temperature for 10 min. Absorbance was measured at 578 nm (5) on a microplate reader (Tecan Safire2^{TM}). All reagents were prepared for same day use, and calibration curves were performed for each plate tested. A calibration curve using a calcium standard is shown in Fig. S15a.

The Limit of Blank (LoB) for the *o*–cresolphthalein complexone assay was calculated using:

$$\mathrm{LoB} = \bar{x}_{\mathrm{Blank}} + \sigma_{\mathrm{Blank}}$$

where PBS served as the blank and a negative control throughout the experiment ($n = 60$ used for $\bar{x}_{\mathrm{Blank}}$ and σ_{Blank}). The Limit of Detection (LoD) was determined by:

$$\mathrm{LoD} = \mathrm{LoB} + 1.645 * \sigma_{\mathrm{Low\ Concentration\ Sample}}$$

where the low concentration sample was a 1 mM calcium standard ($n = 60$ used for $\sigma_{\mathrm{Low\ Concentration\ Sample}}$) (6). The GO pellets had poor water stability, often disintegrating into dispersions on the order of minutes; thus, graphene oxide (GO) pellets were run as an additional negative control to demonstrate free graphenic particles did not interfere with the assay. Fig. S15b displays the LoB, LoD, and GO sample absorbance obtained from the *o*–cresolphthalein complexone assay.

Calcium Elution Model: The Korsmeyer–Peppas mathematical model was employed to determine the mechanism of calcium diffusion from CaPG scaffolds. This mathematical model can be applied to cylindrical scaffolds that do not structurally degrade or erode as the target drug is eluted (7). In our experiment, CaPG pellets were cylindrically shaped and did not appear to structurally degrade or erode during the experiment. Thus, calcium elution from CaPG scaffolds was fit to the Korsmeyer–Peppas mathematical model using the following equation:

$$\left(\frac{C_t}{C_\infty} * 100\right) = kt^n$$

where C_t is concentration of calcium at time t, C_∞ is the total calcium concentration, k is the rate constant, t is time, and n is the release exponent (7). To determine C_∞, we used the wt.% of calcium determined via XPS for CaPG pellets (10.0 %), mass of the pellets (~25 mg), and a sample volume (1 mL). The upper limit of calcium present in the CaPG scaffolds was calculated by:

$$(0.10 \times 25\ \text{mg}) \times \frac{1\ \text{g}}{1000\ \text{mg}} \times \frac{1\ \text{mol Calcium}}{40.078\ \text{g Calcium}} \times \frac{1000\ \text{mmol Calcium}}{1\ \text{mol Calcium}} \times \frac{1}{0.001\ \text{L PBS}} = 62.4\ \text{mM}$$

and denoted as C_∞.

The model only provides a linear fit if less than 60% of the total drug has been eluted. In our experiment, calcium elution plateaued after fourteen days at ~18% total calcium content; therefore, the first fourteen days of the experiment were used to calculate the release exponent. For cylindrical scaffolds, when $n \leq 0.45$, the drug release mechanism is diffusion controlled (7). We calculated a release exponent of 0.42 (Fig. S16d), indicating diffusion-controlled calcium elution from CaPG pellets.

***In vitro* Phosphate Elution Study.**

Experimental Design: A 50 mM Tris buffer was prepared at a pH of 7.7 at room temperature (results in a pH of ~7.4 at 37 °C). To mimic the ionic environment of the Ca^{2+} elution experiment, NaCl and KCl were added to the buffer at a final concentration of 137 mM and 2.7 mM, respectively. GO pellets and CaPG pellets were then submerged in 1 mL of 50 mM Tris buffer in 15 mL centrifuge tubes. Tris buffer negative controls (n = 3) were also run during the experiment. All samples were stored at 37 °C throughout the experiment (14 days) and run in triplicate. Zero–time points were acquired by aliquoting immediately after pellets were submerged in Tris buffer equilibrated to 37 °C. Time points were obtained by aliquoting 75 μL of sample. Phosphate quantification was determined using the PiPer™ Phosphate Assay Kit acquired from ThermoFisher Scientific.

PiPer™ Phosphate Assay: Phosphate quantification was determined using the product protocol. That is, P_i standards were prepared from a 50 mM phosphate standard in 1× Reaction Buffer. Then, 50 μL of samples and controls were added to 96 well cell culture plates. A working solution of 100 μM Amplex Red was prepared that contained 4 U mL^{-1} maltose phosphorylase, 0.4 mM maltose, 2 U mL^{-1} glucose oxidase, and 0.4 U mL^{-1} horseradish peroxidase. The Amplex Red solution was used immediately by adding 50 μL into each well containing samples and controls. The plate was then incubated for 30 min at 37 °C and measured on a microplate reader. Phosphate quantification can be determined via fluorescence or absorbance. Since experimental samples were concentrated, absorbance was used for quantification at 570 nm. A calibration curve of phosphate is shown in Figure S15c.

A LoB and LoD were not determined experimentally since the kit was purchased commercially. Further, GO pellets in Tris buffer were also run as an additional negative control to

ensure trace graphenic materials in supernatants did not interfere with the assay. The absorbance of GO and the Tris buffer throughout the course of the experiment are shown in Figure 15d.

Dynamic Light Scattering (DLS). Samples were prepared for DLS by diluting PG powders in DI water to 100 μg mL^{-1}. Since graphenic powders that are lyophilized to dryness form a powder that readily enables self-interaction, there tends to remain some large flocculants after addition of DI water. Sonication is widely used to disperse graphenic materials suspended in a liquid. Thus, brief (~10 s) bath sonication (240 W, 42 kHz, ultrasonic cleaner, Kendal) was used to disperse flocculants. Even though sonication was successful at dispersing large flocculants, the dispersions are not kinetically stable, as they undergo sedimentation and formation of new flocculants. To minimize these effects during DLS analysis, the dispersions were agitated via pipetting before each measurement to ensure a uniform mixture.

A Zetasizer Nano ZS (Malvern Instruments Ltd., Worcestershire, UK) was used to perform DLS using Zetasizer Software v7.12 (Malvern, Inc.). Five measurements consisting of 10 scans of 10 s each were acquired in backscatter (173°) mode. The instrument automatically determined the best attenuation factor and measurement position. The mean count rate was ~200 kcps.

The instrument measures scattering intensity over time, and the correlator calculates the correlation function, $G(\tau)$, of the scattered intensity, I:

$$G(\tau) = \langle I(t)I(t+\tau)\rangle$$

where τ is the time difference. For particles undergoing Brownian motion, the correlation function will have the form of an exponential decay:

$$G(\tau) = A[1 + Be^{-2\gamma\tau}]$$

where *A* and *B* are constants and

$$\gamma = Dq^2$$

where *D* is the diffusion coefficient and

$$\mathrm{q} = \frac{4\pi n}{\lambda}\sin\frac{\theta}{2}$$

where *n* is the index of refraction, λ is the laser wavelength, and θ is the scattering angle. For polydisperse samples, there will be numerous exponentials for each particle size, and the equation can be written as follows:

$$G(\tau) = A[1 + Bg_1(\tau)^2]$$

where $g_1(\tau)$ is the sum of all exponential decays in the correlation function.

In the Cumulants analysis, the software fits a single exponential to the correlation function and calculates a particle size from *D*:

$$D = \frac{k_B T}{6\pi\eta r}$$

where k_B is the Boltzmann constant, *T* is absolute temperature, η is dynamic viscosity, and *r* is the radius of a spherical particle. This value is the "Z-Average diameter", which is also known as the "Cumulants mean" or "scattered light intensity-weighted harmonic mean particle diameter".

Furthermore, in the Cumulants analysis, an estimate of the width of the distribution is calculated and called the "polydispersity index". It is dimensionless and scaled such that values < 0.05 are for highly monodisperse samples and values > 0.7 indicate a very broad size distribution.

For data reporting, we calculated the mean and standard error of the mean of the five measurements of the Z-average diameter. Note that although the polydispersity index is very

high (~1), determinations of the Z-average diameter were reasonably consistent between samples. In a similar manner, we calculated the mean and standard error of the mean of the five measurements of the polydispersity index. To report the as-acquired raw data, we show the average correlograms for each material.

Zetasizer Software was also used to calculate the volume and number distributions. The fundamental DLS intensity distributions were converted using proprietary Malvern Inc. algorithms based on Mie theory and four assumptions: all particles are spherical, all particles are homogeneous, the optical properties of the particles are known, and there is no error in the intensity distribution. Since graphenic materials do not fulfill all of these criteria and the DLS technique inherently leds to peak broadening, the volume and number distributions are only included for comparative purposes and should not be considered accurate representations of particle diameters.

As a complementary technique to assess particle size, we performed high-resolution optical microscopy and imaging, as described below.

Particle Imaging. Dispersions of PG powders were prepared as described in the section on DLS. Aliquots of 20 μL were drop cast onto #1.5 microscopy coverslips and allowed to dry at 37 °C. The coverslips were secured onto microscopy slides using tape at the edges to avoid artifacts from mounting media, adhesives, *etc*. Bright field, color optical imaging of PG materials was performed on an EVOS® FL Auto Cell Imaging System (ThermoFisher Scientific) with a 100×, 1.40 numerical aperture, oil-immersion objective. For this imaging system, a single pixel corresponds to a length of 90 nm. ImageJ (National Institutes of Health, Bethesda, Maryland) was used to intensity threshold the images and then automatically detect and analyze particles. To exclude noise and artifacts, only particles of size ≥ 9 pixels^2 (corresponding to particles with diameters > ~300 nm) were quantified. Sample means, standard deviations, and standard errors of the means were calculated from at least 400 particles. These data sets were also used to generate histograms of the distributions of particle sizes.

Zeta Potential. Samples for Zeta potential experiments were prepared in the same way as described for DLS. Dispersions of graphenic materials were loaded in Malvern disposable folded capillary cells (DTS1070), and a Zetasizer Nano ZS with Zetasizer Software v7.12 (Malvern, Inc.) was used to determine zeta potential. Five measurements were acquired using the optimal scanning parameters of the instrument (ranging from 10–100 scans per measurement).

Cell Culture. All cell culture reagents were acquired from ThermoFisher Scientific. NIH–3T3 murine fibroblasts and RAW 264.7 murine macrophages were cultured in Dulbecco's Modified Eagle Medium with concentrations of 4,500 mg L^{-1} for D–glucose, 584 mg L^{-1} of L–glutamine, and 100 mg L^{-1} sodium pyruvate (#11995065). This basal media was supplemented with 10% v/v calf serum (#16010159) and 10% v/v fetal bovine serum (#26140079) for the NIH–3T3 and RAW 264.7 cells, respectively. Both medias were also supplemented with penicillin-streptomycin (#15140122) that was diluted to a final concentration of 100 U mL^{-1}. The cells were cultured at 37 °C with a humidified atmosphere at 5% CO_2.

Adipose–derived hMSCs (#R7788–115) were cultured in commercially available, reduced–serum growth media that is optimized for hMSC expansion and preservation of potency: MesenPRO RS™ Medium (#12746012) supplemented with L–glutamine (#25030081) diluted to 2 mM and penicillin/streptomycin (#15140122) diluted to 100 U mL^{-1}. Osteogenic

media is a commercially available formulation designed for complete osteogenic differentiation of hMSCs: StemPro® Osteogenesis Differentiation Kit (#A1007201) supplemented with gentamicin (#15710064) diluted to 5 μg mL^{-1}. For subculture, hMSCs were detached using TrypLE™ Express without phenol red (#12604013) due to its high level of purity that reduces cellular damage from non–specific reactions. All hMSC reagents were free from phenol red since phenol red affects osteogenic differentiation (8). To ensure potency, hMSCs were not used beyond passage five.

Cellular Vitality Analysis. Powders of material were suspended in sterile DI water at concentrations of at least 1 mg mL^{-1} and sterilized via exposure to 254 nm ultraviolet light for 10 min. For the counter ion cytocompatibility experiment, the anion associated with each cation was chloride, and the cellular exposure concentrations were based on the mass concentration of the cation. For the PG materials, the cellular exposure concentration was based on the total mass of the PG material. These dispersions were diluted to the final, indicated concentration in complete cell culture media.

NIH–3T3 fibroblasts and RAW 264.7 macrophages were seeded in the interior wells of 96–well plates at a density of at 3×10^4 and 2×10^4 cells cm^{-2}. After 8 h, the cells were well adhered, and the media was exchanged for media containing the experimental samples. Since different exposure concentrations required different volumes of the stock suspensions of PG materials, deionized water was added as appropriate to ensure that all wells were diluted by the same volume. Control cells were exposed to deionized water at the same volume. The final dilution of cell culture media was < 2% v/v. Cells were allowed to grow for 48 h, approaching the end of the log growth phase at which point the assays have the highest sensitivity, and then the vitality assays were performed.

We assessed cellular enumeration, vitality, and late necrosis and apoptosis using fluorescent reporters. To do so, we aspirated the cell culture media that contained the experimental samples, washed the cells with PBS (#10010049, ThermoFisher Scientific), and exposed the cells to 20 μM of Hoechst 33342 (#62249, ThermoFisher Scientific); 5 μM of Calcein AM (#PK–CA707–80011–2, PromoKine); and 2.5 μM of ethidium homodimer–1 (#L3224, ThermoFisher Scientific) for 15 min. Hoechst 33342 labels the DNA of all cell nuclei and then becomes brightly fluorescent, reporting the number of cells. Upon cellular internalization of Calcein AM, it is converted to a fluorescent form by esterases, reporting vitality. Ethidium homodimer–1 becomes brightly fluorescent upon binding DNA but is excluded from the nuclei of live cells; thus it reports dying cells that have not yet detached from the substrate. To quantify the fluorescence of these molecules, we used a fluorescence microplate reader with excitations of 350/20 nm, 483/20 nm, and 525/20 nm and emissions of 461/20 nm, 525/20 nm, and 617/20 nm for Hoechst 33342, Calcein AM, and ethidium homodimer–1, respectively. Since graphenic materials may alter fluorescence assays, we also performed direct fluorescence imaging using an EVOS® FL Auto Cell Imaging System with a 10×, 0.30 numerical aperture objective.

Optical Imaging. NIH–3T3 fibroblasts and RAW 264.7 murine macrophages were seeded into 48–well plates at 3×10^4 and 2×10^4 cells cm^{-2}. After 8 h, PG materials that were dispersed in water at 5 mg mL^{-1} were added to the cell culture media, being diluted to 10 μg mL^{-1}. Cells were exposed to PG materials for 48 h; then they were exposed to Hoechst 33342 at 20 μM and MitoTracker® Red CMXRos (#M7512, ThermoFisher Scientific) at 100 nM for 30 min in cell

culture media to label DNA and mitochondria, respectively. The cells were then washed three times with PBS and fixed with 3.7% v/v formaldehyde in PBS for 15 min. The cells were then washed three more times and exposed to 0.2% v/v Triton X–100 for 5 min. After three more washes with PBS, the cells were exposed to Acti–stain™ 488 phalloidin (#PHDG1, Cytoskeleton, Inc.) at 100 nM for 1 h. After three final washes with PBS, the cells were maintained in PBS to which SouthernBiotech Fluoromount–G™ mounting medium (OB100–01, Fisher Scientific) was added at 5% v/v. Cells were imaged using a 40×, 0.65 numerical aperture, long working distance objective.

Confocal imaging was performed with a Zeiss LSM 880 confocal microscope with a 100×, 1.4 numerical aperture, oil–immersion objective. A laser line of 405 nm was used for Hoechst 33342 fluorescence and for quasi–differential interference contrast for cellular structures. A laser line of 488 nm was used for Calcein AM fluorescence. Z–stacks were acquired with a 500 nm step size, and maximum projections and overlays were created in ZEN Blue Edition© (Carl Zeiss MicroImaging GmbH).

ALP and ARS Quantification. hMSCs were seeded into 96–well plates, cultured for 1 day, and then exposed to the indicated experimental conditions (*i.e.*, growth or osteogenic media with or without PG materials). ALP and ARS expression was assayed over 1–28 days of cellular exposure. The cellular media was changed biweekly. Since ~90% of the PG materials remained associated with the hMSCs after the first 3.5 days of exposure, subsequent media exchanges were not spiked with PG materials to prevent smothering the cells.

ALP: ALP was quantified using the ImmPACT™ Vector® Red Alkaline Phosphatase kit (#SK–5105, Vector Laboratories, Inc.) according to the manufacturer's protocol. The hMSC media was aspirated, and the cells were washed with PBS. Then, the hMSCs were fixed with 3.7% formaldehyde v/v for 10 min. The formaldehyde solution was aspirated, the cells washed with PBS, and to each well 50 μL of ImmPACT™ Vector® Red substrate working solution spiked with Hoechst 33342 at 20 μM was added and incubated for 1 h. After labeling, the cells were washed with PBS for 5 min. Then, the PBS was aspirated, and 200 μL of fresh PBS was added per well. Then, the signal was quantified using a fluorescence microplate reader: Hoechst 33342 fluorescence with an excitation of 350/20 nm and an emission of 461/20 nm; absorbance spectra from 250 to 800 nm with a 10 nm step size of the ImmPACT™ Vector® Red reaction product (peak maximum ~500 nm), and fluorescence of the ImmPACT™ Vector® Red reaction product with an excitation of 550/20 nm and an emission of 650/20 nm. Quantification of spectroscopic data was performed by subtracting the baseline absorbance at 700 nm from the ALP absorbance at 500 nm, averaging experimental replicates together, and normalizing to the media controls. Additionally, since graphenic materials are highly optically absorbing and, especially at longer time points, the cellular distribution may not be uniform throughout the well, we performed optical microscopy, imaging the entire well with a 10×, 0.30 numerical aperture objective in bright–field mode with a color focal plane array detector (EVOS® FL Auto Cell Imaging System, ThermoFisher Scientific). To probe the cellular/sub–cellular distribution of ALP expression, we also performed higher–magnification imaging using a long–working distance 40×, 0.65 numerical aperture objective. To quantify ALP expression from the whole–well microcopy images, we converted the RGB color images to CIE 1976 (*L*a*b**) format using MATLAB (MathWorks®). Pixels with a value of at least 15 for the a* channel were considered to represent regions that were stained red for ALP expression. From these thresholded images, the

total a* pixel intensity was calculated. The results were averaged across whole–well images from multiple wells and normalized to the growth or osteogenic media controls.

ARS: ARS (#97062–616, VWR) was diluted to 40 mM in DI water, had a pH of 4, and was used to assay for calcium deposition. The hMSC media was aspirated, the cells were washed with PBS without calcium and magnesium that was used for all the cellular experiments (#10010023, ThermoFisher Scientific), and the cells were fixed with 3.7% formaldehyde v/v for 10 min. Then, the formaldehyde solution was aspirated, and the cells were washed with PBS and exposed to 100 μL per well of 40 mM ARS solution in DI water for 30 min. After labeling, the cells were washed five times with PBS and then maintained in 200 μL of PBS. To determine ARS labeling, absorbance spectroscopy from 250 to 800 nm with a 10 nm step size was performed using a fluorescence microplate reader. To confirm the spectroscopic results and determine the cellular and sub–cellular distribution of the ARS labeling, whole–well (10×) and higher magnification (40×) imaging was performed.

To quantify ARS labeling, the background absorbance at 800 nm was subtracted from the ARS absorbance at 550 nm, data from multiple wells were averaged together, and the samples were normalized to the growth or osteogenic media controls. For some wells of hMSCs exposed to KPG, MgPG, and NaPG for 28 days, the primary masses of cells had localized themselves to the environs of the wells; thus, the spectroscopic results were not accurate, and these wells were excluded from analysis. For KPG, the valid number of data points for day 28 is $n = 1$, and that value is reported as the bar. Its error bar represents the sample standard deviation of $n = 3$ samples that were exposed to KPG for 21 days that was then scaled to the value at day 28. For MgPG, the number of valid samples is $n = 0$. To approximate the response, the percent increase in ARS signal from day 21 to day 28 was calculated for GO, KPG, LiPG, and NaPG. This average scaling was applied to the MgPG mean from day 21 to approximate the value at day 28. The error bar was calculated by applying the same scaling to the sample standard deviation at day 21 for MgPG. For NaPG, the number of valid samples is $n = 2$. The bar is the mean of those two samples, and its error bar represents the sample standard deviation of those two values.

RT–qPCR. A one–step method was used for reverse transcription quantitative polymerase chain reaction (RT–qPCR) since it requires smaller sample sizes and minimizes sample loss. A CellsDirect™ One–Step qRT–PCR Kit with ROX (#11754100, ThermoFisher Scientific) was used to lyse the hMSCs and stabilize the RNA. Reverse transcription and PCR amplification were performed using qScriptTM XLT One–Step RT–qPCR ToughMix®, ROX™ (#95133–100, Quanta BioSciences™) on an Applied Biosystems 7300 instrument. Commercially available hydrolysis probe TaqMan® gene expression assays were used for quantitative PCR amplification of RNA for bone morphogenetic protein 2 (BMP–2), collagen type I alpha 1 (COL1A1), runt–related transcription factor 2 (RUNX–2), small nuclear ribonucleoprotein D3 (SNRPD3), and proteasome subunit beta 2 (PSMB2) (#Hs01055564_m1, #Hs00164004_m1, #Hs00231692_m1, #Hs00188207_m1, and Hs00267650_m1, ThermoFisher Scientific).

All PCR plastic consumables were certified DNase, RNase, and pyrogen free, and the pipettes tips contained aerosol filters and were purchased sterilized (*via* γ–irradiation). All PCR work was performed in a sterilized environment. For one–step RT–qPCR, lysis was based on the recommendations of the CellsDirect™ One–Step qRT–PCR Kit with ROX (#11754100, ThermoFisher Scientific). Briefly, hMSCs were cultured in 96–well plates for 14 days, at which time there were ~15 000 cells well^{-1}. Then, the media was aspirated, the cells washed with PBS, and 22 μL of lysis solution master mix was added to each well for 10 min. After 10 min, the

majority of cells were detached and/or burst, and the plate was mechanically tapped and the wells vigorously scrapped to finalize the lysis procedure. Then, the lysates from each well were placed into separate 0.65 μL microcentrifuge tubes and placed into an incubator at 75 °C for 10 min. Afterwards, the Mg^{2+} concentration was adjusted by the addition of 2 μL of 50 mM $MgSO_4$ to each tube. Since each of the hydrolysis (TaqMan®) primer/probes spans an exon junction, the DNase I digestion step was omitted to prevent RNA hydrolysis. Then, the samples were flash frozen in liquid nitrogen and stored in liquid nitrogen vapor phase until use in RT–qPCR.

RT–qPCR experiments were run in sealed (#60941–070, VWR) 96–well PCR plates (#82006–644, VWR). Master mixes were made for all components as appropriate, and the reaction volume was 10 μL. For each reaction, there was 5.00 μL of qScript™ XLT One–Step RT–qPCR ToughMix®, ROX™ (#95133–100, Quanta Biosciences™: containing 2× reaction buffer containing dATP, dCTP, dGTP, dTTP, magnesium chloride, qScript XLT reverse transcriptase, RNase inhibitor protein, hot–start DNA polymerase, AccuVue blue qPCR dye, ROX Reference Dye and stabilizers), 0.50 μL of the TaqMan® primer/probe (20× mix diluted to final concentrations of the forward primer, reverse primer, and probe of 900, 900, and 250 nM, respectively), 3.5 μL of DPEC–treated water (#AM9906, ThermoFisher Scientific), and 1.00 μL of 10× diluted lysate master mix. Since the CellsDirect™ One–Step qRT–PCR Kit with ROX it is a one–step kit, sample amounts are based on the total number of cells, and the kit is designed to work over a range of 1 to 10 000 cells per reaction. Thus, for each PCR experiment, a lysate master mix was prepared by diluting the stock lysate (~15 000 cells per 22 μL) in DPEC–treated water to the desired cell number. For the best PCR efficiency, samples were run in the range of ~100 cells per reaction (see details below). The commercially available TaqMan® primer/probes for BMP–2, COL1A1, and RUNX–2 (#Hs01055564_m1, #Hs00164004_m1, and #Hs00231692_m1, ThermoFisher Scientific) had a FAM reporter dye while the reference gene SNRPD3 and PSMB2 (#Hs00188207_m1 and Hs00267650_m1, ThermoFisher Scientific) had a VIC reporter dye. Amplicon lengths were 84, 66, 116, 68, and 80 for BMP–2, COL1A1, RUNX–2, SNRPD3, and PSMB2, respectively, and all spanned an exon junction. Reverse transcription/cDNA synthesis and real–time PCR was performed on an Applied Biosystems 7300 instrument controlled by Sequence Detection Software Version 1.4: reverse transcription/cDNA synthesis, 50 °C for 10 min; initial denaturing, 95 °C for 1 min; 70 cycles of PCR, 95 °C for 15 s followed by 60 °C for 60 s. The Sequence Detection Software was used to calculate and plot ΔRn and to automatically calculate a baseline and threshold to determine the threshold cycle (C_T), also referred to as quantification cycle.

Experimental samples were not multiplexed as it resulted in less precise data likely due to competition for reagents. Also, RT–qPCR was attempted with the components of the CellsDirect™ One–Step qRT–PCR Kit with ROX kit that included SuperScript® III RT/Platinum® Taq Mix (with RNaseOUT™ Ribonuclease Inhibitor); however, even after numerous attempts with different conditions, it failed to generate data with a realistic amplification efficiency for these samples. Thus, we used the qScript™ XLT One–Step RT–qPCR ToughMix®, ROX™ that led to an efficiency ranging from 372 to 137%, improving with increasing lysate dilution from 1500 to 6 cells. Thus, there were likely PCR inhibitors in the reaction.

To compare gene expression levels, we used the $2^{-\Delta\Delta C_T}$ method, (9) noting that the PCR efficiency was non–ideal but that the same assumption of 100% efficiency was used for both experimental and control samples. The average C_T for each sample for each gene was calculated. Then, the ΔC_T for each sample was calculated by subtracting the C_T of each reference gene from

the experimental gene. The $\Delta\Delta C_T$ was calculated by subtracting the ΔC_T of the growth media control from the ΔC_T of the experimental samples. Fold expression was calculated by $2^{-\Delta\Delta C_T}$. Finally, the two sets of data for each reference gene were averaged together. Error bars are standard error propagated through the $2^{-\Delta\Delta C_T}$ method using the derivative method of error propagation. Note that the error bars are not symmetrical since $2^{-\Delta\Delta C_T}$ is not linear.

Cellular Growth on PG Materials. To create quasi–substrates of PG materials, we drop cast concentrated dispersions of PG materials onto #1.5 microscope coverslips. We allowed the water to evaporate, creating a layer of PG materials on the coverslips. These substrates were sterilized by immersion in 70% ethanol for 10 min, followed by aspiration and washing three times with PBS. During these steps, some of the mass of the substrates was dislodged; regardless, some mass remained. These coverslips containing regions of PG substrates were placed into cell culture dishes, and NIH–3T3 fibroblasts were added to the entire dish and cultured for 24 h. After 24 h, the cells were exposed to Hoechst 33342 and Calcein AM as described above. Then, the labeling solution was aspirated, the cells washed with PBS, and fixed with 3.7% formaldehyde for 10 min. After fixation, the cells were washed and the coverslips mounted onto microscopy slides for confocal imaging.

To assess cellular growth on 3–D constructs, PG pellets of 3.75 mm diameters were placed into 48–well (well diameter of 11.05 mm) cell culture plates. PG pellets were sterilized with exposure to 254 nm ultraviolet light for 5 min. Passage number three hMSCs were diluted in 500 μL of complete MesenPRO RS™ Medium and added to the entire well, covering the pellet. The media was exchanged after 3.5 days of culture. After 7 days, the cells were fixed and labeled with Hoechst 33342, Acti–stain™ 488 phalloidin, and MitoTracker®, as described above. To enable imaging of cells on our inverted microscope, the pellets were picked up with tweezers, flipped, and placed cell–side down into a fresh well with PBS. Images were acquired using a 10×, 0.30 numerical aperture objective, and images of entire pellets were obtained using the automatic imaging and concatenation feature of the EVOS® FL Auto Cell Imaging System. Individual, higher–resolution fields of view were imaged with a 40×, 0.65 numerical aperture, long working distance objective.

Bone marrow stromal cell isolation. All aspects of the animal protocol were approved by UConn Health Institutional Animal Care and Use Committee (IACUC). All mice used in this study were constructed in the laboratory of Dr. David Rowe at UConn Health. They were generated, bred, and maintained at the Center for Laboratory Animal Care of UConn Health. The animals had free access to sterile water and standard rodent chow *ad libitum*.

CD–1 transgenic mice containing the 3.6–kb fragment of the rat collagen type 1 promoter fused to a cyan fluorescent protein (Col3.6Cyan) were used to derive bone marrow stromal cells. Mice between the ages of 7–8 weeks were sacrificed by CO_2 asphyxiation followed by cervical dislocation. The femurs and tibias were carefully isolated and dissected from the surrounding soft tissue. The two ends were cut and the bone marrow was collected by flushing complete media consisting of high glucose DMEM with L–Glutamine (#12604, Lonza), 10% FBS, and 1% penicillin/streptomycin with a 25 gauge needle. When all the marrows were obtained, the suspension was passed through an 18.5 gauge needle. After counting, the cells were plated in a 100 mm dish at a density of approximately 6×10^7 cells per dish. Cells were kept in a Sanyo incubator under low oxygen conditions. At day 3 and 6, the media was replaced with fresh complete media. At day 7, the cells were washed with PBS, detached with Accutase, and

resuspended in complete media at a concentration of 1×10^6 mL^{-1}. Prior to injections, the cells were centrifuged. The media was removed and replaced with 50 μL of PBS containing either GO, CaPG, or GO+rhBMP–2.

Surgical procedure. Animal studies were performed in accordance with protocols approved by IACUC at UConn Health. Col3.6 fluorescent protein reporter mice expressing two distinct fluorescent proteins (topaz and cyan) were used to understand the contribution of the host and donor cells in ectopic bone formation. These mice were generated, bred, and maintained at the Center for Laboratory Animal Care of UConn Health and had access to food and water *ad libitum*.

CD–1 transgenic mice containing the 3.6–kb fragment of the rat collagen type 1 promoter fused to a topaz fluorescent protein (Col3.6Topaz) or NOD.Cg–*Prkdc*^{scid} *Il2rg*^{tm1Wjl}/SzJ (NOD *scid* gamma, NSG) immunodeficient mice containing the 3.6–kb fragment of the rat collagen type 1 promoter fused to a topaz fluorescent protein (NSG/Col3.6Topaz) were used for subcutaneous injections. Mice that were 11 weeks old were anesthetized through a nose cone under 1.5% isoflurane. Their backs were shaved and cleaned with 70% ethanol pads. GO or CaPG dispersions (0.54 mg, which approximates 20 mg kg^{-1} body weight) were injected subcutaneously in 50 μL of PBS, using 27 gauge, 0.5 cm^3 insulin syringes. Each mouse received two such injections on either side of the dorsum. In the case of GO+rhBMP–2, each injection site received 2.5 μg of rhBMP–2, combined with GO prior to injection. The NSG/Col3.6Topaz mice received GO or CaPG combined with 1×10^6 BMSCs prior to injection, per injection site.

One day prior to sacrifice, alizarin complexone at a dose of 30 mg kg^{-1} was injected intraperitoneally to mark areas of active mineralization within 24 h of sacrifice.

X–ray imaging. Animals were sacrificed 8 weeks post–injection by CO_2 asphyxiation followed by cervical dislocation. The subcutaneous tissue in and around the injection site was carefully dissected and fixed in 10% formalin. The samples were imaged radiographically at 1× magnification (6 s at 26 kVp) using a digital capture X–ray cabinet (Faxitron LX–60). Quantitative analysis of the formed mineralized tissue was performed by measuring as–acquired image intensity using MATLAB®.

Cryohistology. After X–ray imaging, samples were returned to 10% formalin and fixed at 4 °C. The following day, they were transferred to a 30% sucrose solution in PBS (pH 7.4) and left overnight at 4 °C. The tissues were then positioned in Shandon™ Cryomatrix™ embedding medium and frozen by immersing in a solution of 2–methylbutane, which was pre–cooled over dry ice. After ~5 min, the samples were removed from the solution, allowed to dry, and then stored in airtight plastic bags at –20 °C until sectioning. Cryosections (5 μm) were obtained on a Leica CM3050S cryostat (Leica, Wetzlar) using a disposable steel blade (Thermo Scientific) and transferred to glass slides using a tape transfer process (Cryofilm type IIC (10), Section–Lab Co. LTD). The slides were then prepared with 50% glycerin in PBS as the mounting medium.

Tartrate–resistant acid phosphatase (TRAP) staining. Buffer 1 was prepared by dissolving 9.2 g sodium acetate anhydrous (#S2889, Sigma–Aldrich) and 11.4 g sodium tartrate dibasic dehydrate (#T6521, Sigma–Aldrich) in 1000 mL of water and adjusting the pH to 4.2 with glacial acetic acid. Buffer 2 was prepared by dissolving 40 mg sodium nitrate (#S2252, Sigma–Aldrich) in 1 mL of water. The TRAP reaction buffer contained 7.5 mL of buffer 1 combined with 150 μL of buffer 2.

The substrate solution contained 3.6 mL of the reaction buffer and 45 μL of Elf–97 phosphatase substrate (#E6588, Invitrogen).

In order to stain for TRAP activity, the coverslips were removed by immersing the slides in PBS for 10 min. After three washes with PBS, the slides were blotted dry and incubated with TRAP reaction buffer for 10 min at room temperature. Slides were then drained and covered with TRAP substrate solution followed by ultraviolet light exposure for 5 min at room temperature. The reaction was stopped by rinsing the slides with PBS three times. Next, the slides were blotted dry, covered with 30% glycerol in PBS, and cover slipped.

Alkaline phosphatase (ALP) Staining. ALP buffer contained 100 mM Tris, 50 mM $MgCl_2$, and 100 mM NaCl, at pH 9.5. A solution of 20 mg mL^{-1} Fast Red TR salt (#F8764, Sigma) in water and a solution of 0.1 g mL^{-1} Naphthol AS–MX phosphate (#N4875, Sigma) in N,N–dimethylformamide (#D158550, Sigma–Aldrich) was prepared. The ALP substrate solution was prepared by combining 4 mL of the ALP buffer, 40 μL of naphthol, and 40 μL of the Fast Red TR solutions.

In order to stain for ALP activity, the slides were placed in PBS to remove the coverslips. After three washes with PBS the slides were blotted dry and incubated with ALP buffer for 10 min at room temperature. The ALP buffer was drained and the slides were blotted dry and incubated with the ALP substrate solution for 5 min at room temperature. The slides were then washed with PBS three times and cover slipped with 50% glycerin/DAPI, which was prepared by adding 1 μL of Hoechst 33342 (#62249, Thermo Scientific™) to a 1 mL solution of 50% glycerol in PBS.

Toluidine Blue (TB) Staining. In order to stain for TB, coverslips were removed by placing the slides in water. The slides were then washed with water, blotted dry, and placed in 0.025% Toluidine Blue O solution (#T3260, Sigma–Aldrich) for 5 min at room temperature. Slides were then rinsed in water and stained with Shandon™ Bluing reagent (#6769001, Thermo Scientific™) for 1 min at room temperature. Next, the slides were rinsed in water and coverslipped with 30%/glycerol in water.

Imaging. Fluorescent and brightfield imaging were performed using the Zeiss Axio Scan.Z1 (Carl Zeiss Microscopy) with chroma filters for each distinct fluorophore (10). The sections were then sequentially imaged for differential interference contrast (DIC), fluorescent reporters and alizarin complexone mineralization label (AC label), TRAP staining, ALP staining with DAPI counterstain, and toluidine blue O staining. This sequence was possible because the cryofilm tape adheres to the tissue and allows for the coverslip to be removed between imaging steps without damaging the section (11, 12).

Chroma fluorescent filter sets used for each fluorophore				
Fluorophore	**Chroma Filter Set**	**Bandpass**	**Excitation**	**Emission**
Alizarin Complexone	ET Cy3/TRITC 49004	565	545/25	605/70
Col3.6Topaz	ET YFP 49003	515	500/20	535/30
Col3.6Cyan	ET CFP 49001	455	436/20	480/40
TRAP	ET 49026	470	405/40	550/60
ALP	ET Cy5 49009	626	640/30	690/50
DAPI	ET DAPI 49000	400	350/50	460/50

Statistics. Sample mean and sample standard deviations are reported, and for parameters that result from calculations of data, the uncertainties reported are the sample standard deviations propagated using the derivative method unless otherwise stated. For statistical inference, we calculated the two–sample *t* statistic and degrees of freedom, and we approximated the distribution with a *t* distribution (13). We performed two–sample *t* tests between experimental samples and controls to calculate *p*–values. For data sets with multiple comparisons, we first performed an ANOVA, and if significant differences were detected, we performed a post hoc Sidak t Test (IBM® SPSS® Statistics 23.0.0.0). Significant differences have a two–tailed P value < 0.05.

Supplementary Results and Discussion:

Synthetic incorporation of inducerons. We have developed a universal synthetic scheme to covalently tether polyphosphates onto graphene oxide (GO), generating phosphate graphenes (PGs). Addition of a Lewis acid catalyst enables precise control over polyphosphate loading and counterion identity that was not previously accessible. We have shown that the catalyst is integral in the phosphate modification using deconvolution of XPS C1s spectra of PG synthesized with and without catalyst (Fig. S2). The presence of the P–C peak (283.5 eV) in C1s spectra indicates that phosphate is covalently bound to the GO backbone, (14, 15) enabling us to garner information about the phosphate seeding density. As shown, PG synthesis without the catalyst results in a less functionalized CaPG, and KPG and NaPG cannot be achieved.

We hypothesize that the inclusion of a Lewis acid catalyst activates epoxide moieties to facilitate phosphate functionalization through epoxide moieties on the basal plane of GO. Even still, we found that magnesium containing PG materials were the most difficult to produce synthetically, which may be explained by magnesium's low electropositivity. Increasing the ratio of magnesium salt to GO from 5:1 to 25:1, generated a reproducible functionalization. There was no further enhancement in functionalization by increasing magnesium salt.

Incorporation of inducerons. Characterization demonstrated effective, covalent functionalization: strong absorption over 1200–1000 cm^{-1} in the Fourier transform infrared (FTIR) spectra corresponds to the presence of phosphates. Deconvolution of the FTIR fingerprint region revealed peaks exclusive to PG materials at 1480–1445, 1030–992, 955–930, and 801–775 cm^{-1}, which correspond to P=O, $P–O_{v3}$, $P–O_{v1}$, and P–C vibrations, respectively (16, 17). X–ray photoelectron spectroscopy (XPS) elemental scans confirmed the presences of the selected counterion (Ca^{2+}, K^+, Li^+, Mg^{2+}, or Na^+) and phosphorus in PGs and absences in GO. Additionally, high resolution XPS P2p spectra supported the results of elemental scans. The emergence of a new peak at 283.5 eV for PG materials in XPS C1s spectra corresponds to P–C bonds, (14, 15) and the phosphorus content from elemental scans corroborate the quantification of the P–C signal from C1s spectra. These unique peaks indicate the presence of phosphates and their covalent tethering to GO (Fig. 1 and Figs. S3–S8).

In the XPS C1s spectra of PG materials, there were significant increases in the C=C/C–C peak at 284.8 eV that correspond to the C=C and C–C bonds of the graphene backbone, indicating reduction. Correspondingly, there was a significant reduction in the C–O (alcohol and epoxide groups) and C=O (carbonyl groups) peaks at 286.5 and 287.4 eV, respectively, demonstrating reduction as well as participation in the Arbuzov reaction. TGA of GO shows a well–defined degradation event for the evolution of labile oxygen groups, and PG materials had a clear increase in the onset temperature (T_o) and first derivative peak temperature (T_p) of the degradation event, consistent with P–C bond functionalization and reduction. XRD indicated functionalization due to the presence of expanded interlayer spacing compared to GO, consistent with polymer functionalization (Fig. S10). Furthermore, the diminishment of the GO peak at 11.8° (d_{hkl} = 7.5 Å) and emergence of a broad diffraction peak at ~23° (d_{hkl} = 3.9 Å) suggest that the graphenic backbone is reduced. Since reduced GO has enhanced *in vitro* and *in vivo* compatibility, (18) this reduction serves to further enhance the compatibility and material–tissue interface of PG materials.

Processing into 3–D scaffolds with osteomimetic mechanical properties. TGA revealed that the T_o of GO powders (191 °C) was less than the processing temperature (200 °C), and GO

constructs displayed a 60% reduction in functional group weight loss, which is attributed to labile oxygen functionalities, and a 44% increase in the char wt.% (Fig. S9). FTIR of GO pellets (Figs. S3, S4) also revealed an increase in the intensity of aromatic ring stretches (1575 cm^{-1}), C–H in–plane bending (1185 and 1050 cm^{-1}), and C–H out–of–plane bending (850 cm^{-1}) with respect to the intensity of the hydroxyl stretch (3420 cm^{-1}), (16, 17) and XPS C1s spectra showed an increase in the C=C/C–C peak at 284.8 eV and reduction C–O and C=O peaks at 286.5 and 287.4 eV, respectively (Table S1 and Figs. S7, S8).

PG materials are cytocompatible. GO, the precursor to the PG materials, is generally considered to be cytocompatible and appropriate functionalization can enhance compatibility (19). Additionally, GO degrades in water over time into structures that are similar to humic acid, which is considered to be a natural degradation product of organic matter, (20) and the degradation of GO can be enhanced by enzymes (21, 22). Recently, we have shown that GO and its aqueous autodegradation products are cytocompatible (2). *In vivo*, GO is sufficiently biocompatible (23). Building upon GO's desirable properties, GO has been covalently functionalized for biomedical applications, and we have previously demonstrated that GO covalently functionalized using the Johnson Claisen rearrangement followed by reduction and the polymerization of homopeptides are cytocompatible (24). Thus, we hypothesized that PG materials would also be cytocompatible.

Particle size is an important aspect when designing a biomaterial, where larger particle sizes are typically correlated with increased compatibility (25). Using DLS and direct optical imaging, it was determined that GO and PG dispersions were composed of similarly sized, relatively large particles (Fig. S17).

To determine cytocompatibility, we exposed PG materials to NIH–3T3 fibroblasts and RAW 264.7 macrophages, since fibroblasts and macrophages are important types of cells involved in the host response to biomaterials, (26) and quantified cellular vitality (Fig. S18). PG materials were cytocompatible up to the maximum tested concentration of 100 μg mL^{-1} beyond which material would smother cells artificially affecting compatibility (2, 27). Since the inducerons are bioinstructive, we studied their cytocompatibilities and found that high levels (125 μg mL^{-1}) of free cations, which roughly correspond to the concentrations of bound cations within the pellets, were compatible except for of lithium. To further investigate cellular interactions, we analyzed the important sub–cellular compartments of nuclei, filamentous actin (F–actin) structures, and mitochondria (28) and found that cellular exposure to PG materials did not alter these sub–cellular structures in either fibroblasts and macrophages (Fig. S19) or hMSCs over the course of two weeks at 100 μg mL^{-1} (Fig. S20). Confocal imaging of fibroblasts cultured on top of flocculants of PG materials demonstrated that cells adhered to and grew on the PG materials (Fig. S19). Overall, high concentrations of powders and 3–D constructs of PG materials are cytocompatible.

***In vivo* evaluation of osteoinductivity.** Subcutaneous injection of CaPG and GO resulted in the formation of pseudo–implants (Fig. S21). Histological sections of the subcutaneous tissue revealed cellular migration into the implant after 8 weeks (Fig. S22). There were some TRAP–positive cells present throughout both implants that were most likely macrophages. These cells appeared to be found more in the GO samples. There was no sign of tissue damage, inflammatory response, or a foreign body reaction. Overall, both GO and CaPG appeared to be well–tolerated by the host.

For GO implanted without donor cells, there was cellular infiltration at the site. However, the infiltrated cells did not show ALP activity or AC label, demonstrating the inability of GO to support ectopic bone formation (Fig. S23b).

Injection of CaPG into the subcutaneous tissue without the addition of donor BMSCs did not lead to the formation of mineralized tissue (Fig. S23c). For CaPG implanted with BMSCs, 6 out of 10 implants did not retain the donor cyan and failed to induce osteogenesis ectopically (Fig. 5e). The implant sites showed the presence of some white mineralized tissue along with diffuse AC label. However, lack of ALP active osteoblasts with AC label indicates the possibility of non–specific ectopic mineralization presumably due to the presence of calcium and phosphate ions in the matrix.

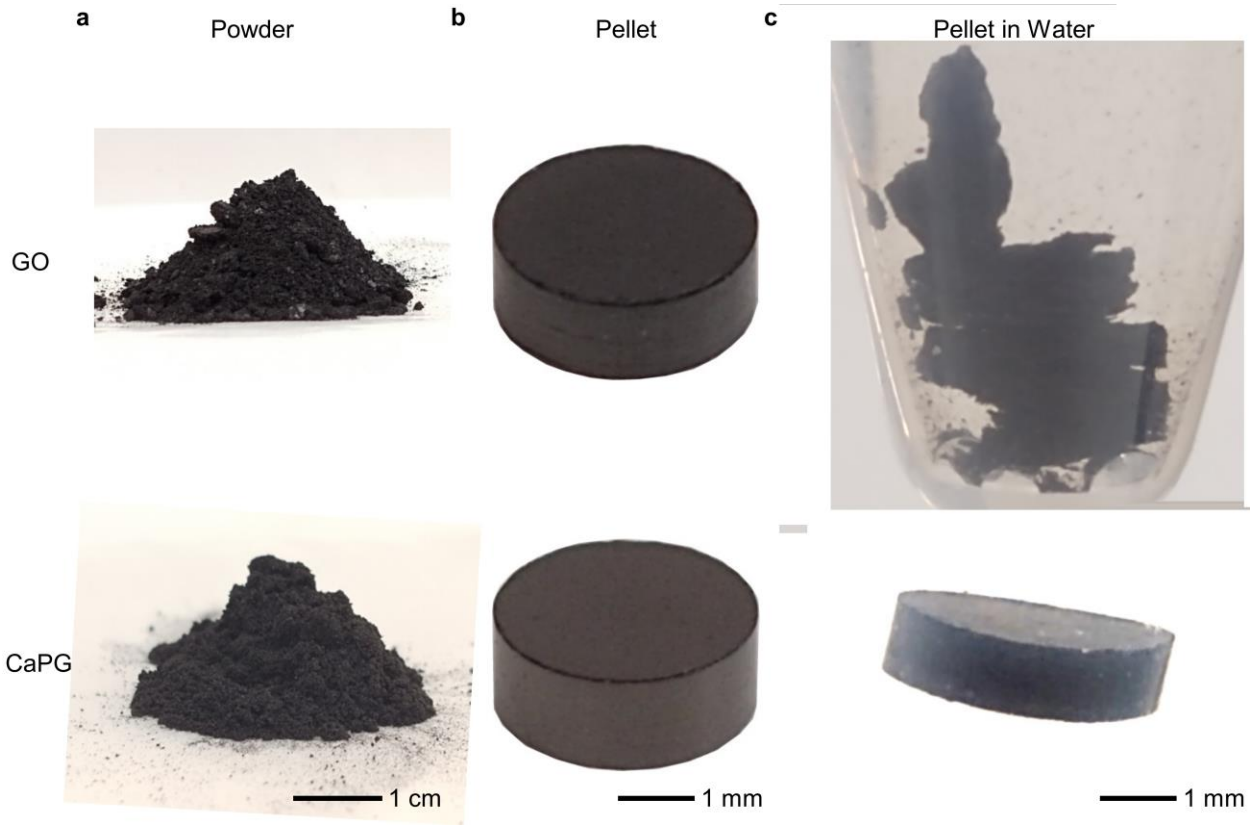

Fig. S1. Representative optical images of PG materials subjected to different conditions. (*A*) As-produced GO and CaPG powders. (*B*) Powders of GO and CaPG that were hot pressed into pellets. (*C*) A GO pellet (top) that was submerged in aqueous solution and immediately lost mechanical integrity and a CaPG pellet (bottom) that was submerged in aqueous solution for 11 days and remained robust.

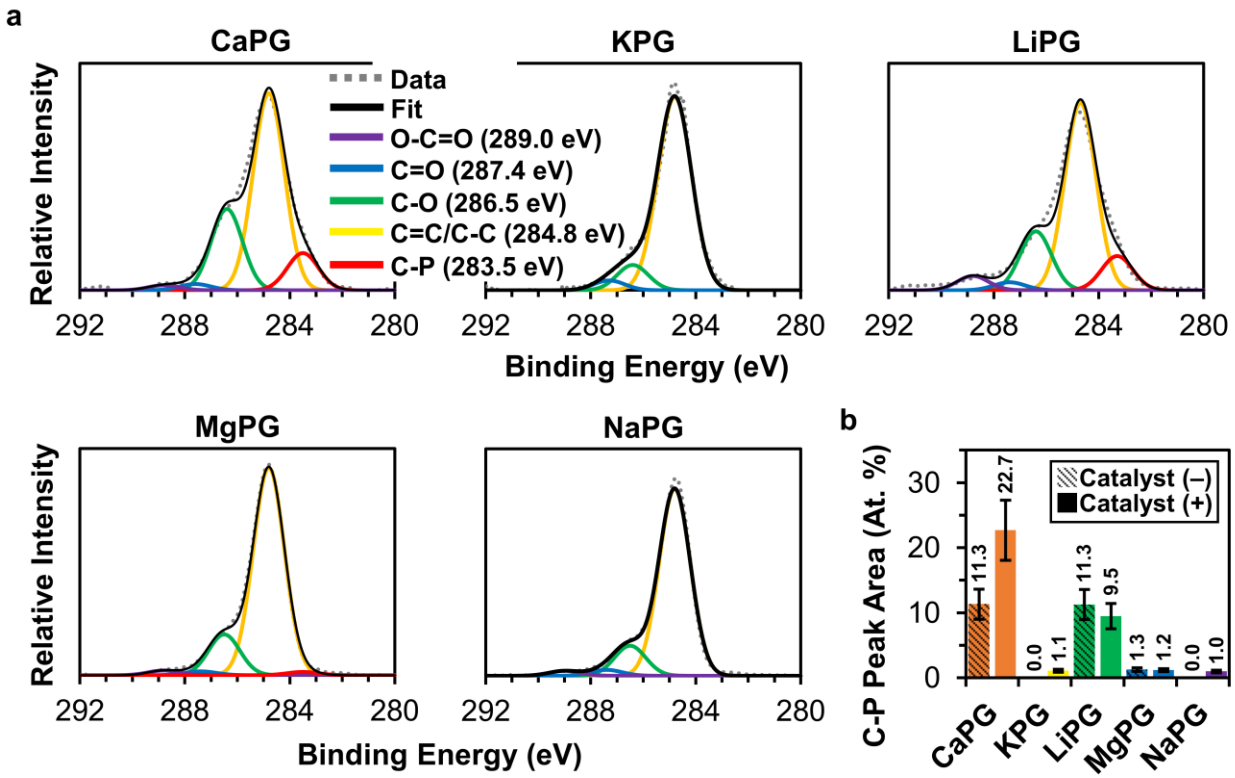

Fig. S2. XPS C1s spectra of PG materials synthesized without the Lewis acid catalyst (magnesium bromide diethyletherate). (*A*) Deconvolution of C1s spectra of PG powders produced without a catalyst, where the C–P peak demonstrates covalent phosphate functionalization on the GO backbone. (*B*) Quantification of the area under the C–P peak for PG materials synthesized with and without catalyst. The error bars represent a relative standard deviation of the C–P peak in the C1s spectra from CaPG powders synthesized with the catalyst (n = 3, where each scan was collected at a different spot on the sample).

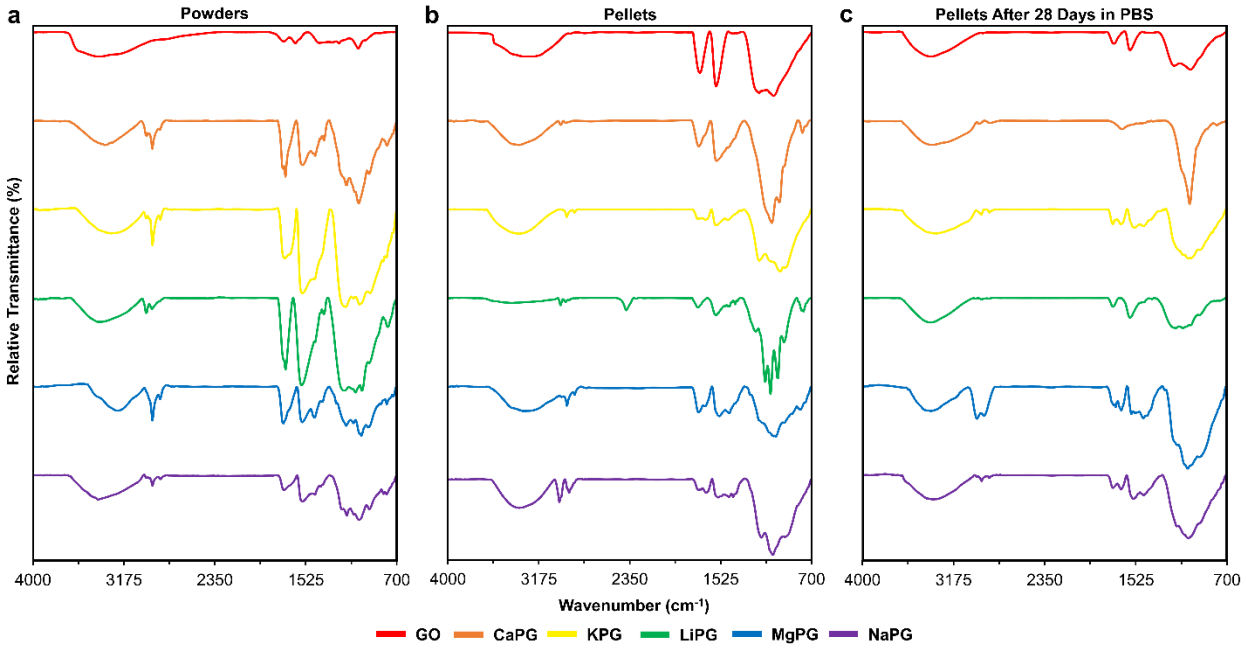

Fig. S3. FTIR spectroscopy of PG materials. FTIR spectra of (*A*) powders, (*B*) pellets, and (*C*) pellets after 28 days in PBS at 37 °C. All spectra were processed as described in the methods (except LiPG pellet because the phosphate stretches exceeded an absorbance of 1.0) and offset for clarity.

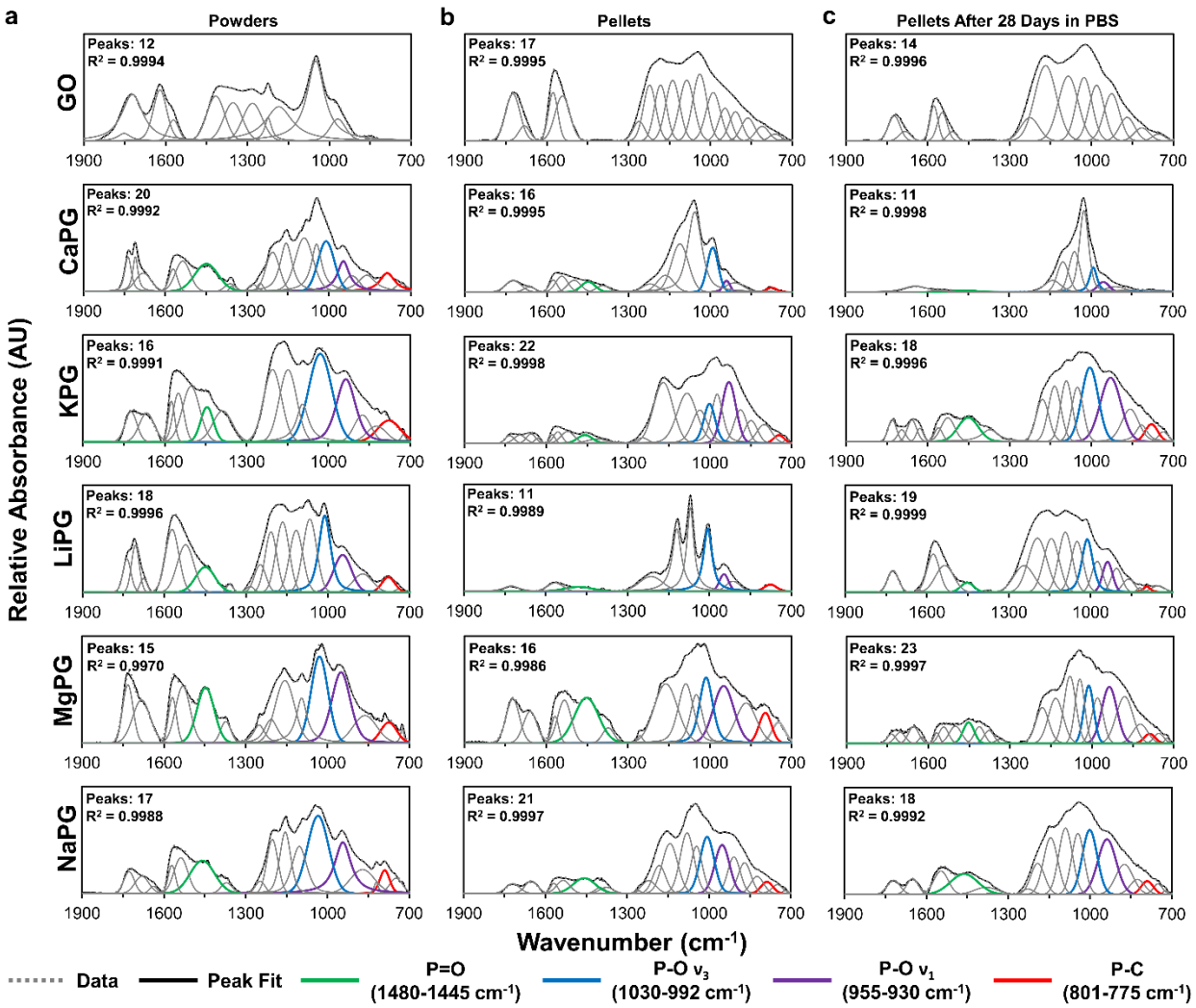

Fig. S4. Deconvoluted FTIR spectra of PG materials. FTIR spectra of (*A*) powders, (*B*) pellets, and (*C*) pellets after 28 days in PBS at 37 °C. All FTIR spectra were normalized as described in the methods (except LiPG pellet because the phosphate stretches exceeded an absorbance of 1.0) and deconvoluted using PeakFit, where deconvolution constraints were also described in the methods. The number of peaks, the R^2 of the peak fit, and phosphate peaks unique to PG materials for P=O (green), P–O $_{v3}$ (blue), P—O $_{v1}$ (purple), and P–C (red) are displayed.

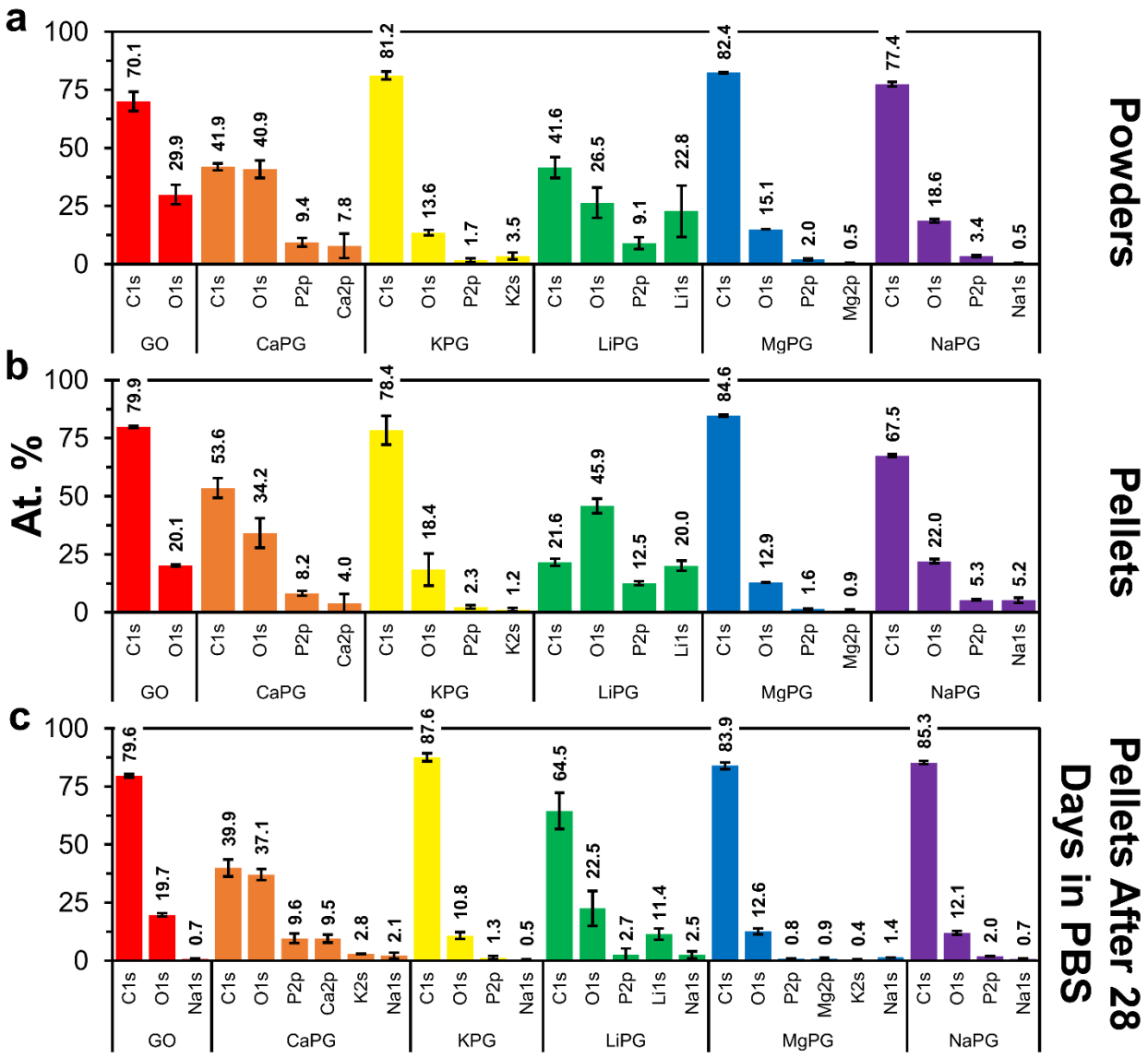

Fig. S5. XPS Elemental composition of PG materials. Elemental composition determined from XPS survey scans of (*A*) powders, (*B*) pellets, and (*C*) pellets after 28 days in PBS at 37 °C. All elemental compositions were quantified as described in the methods. Bars and numerical labels represent $n = 3$ measurements at different spot locations for each material and error bars are the standard deviation.

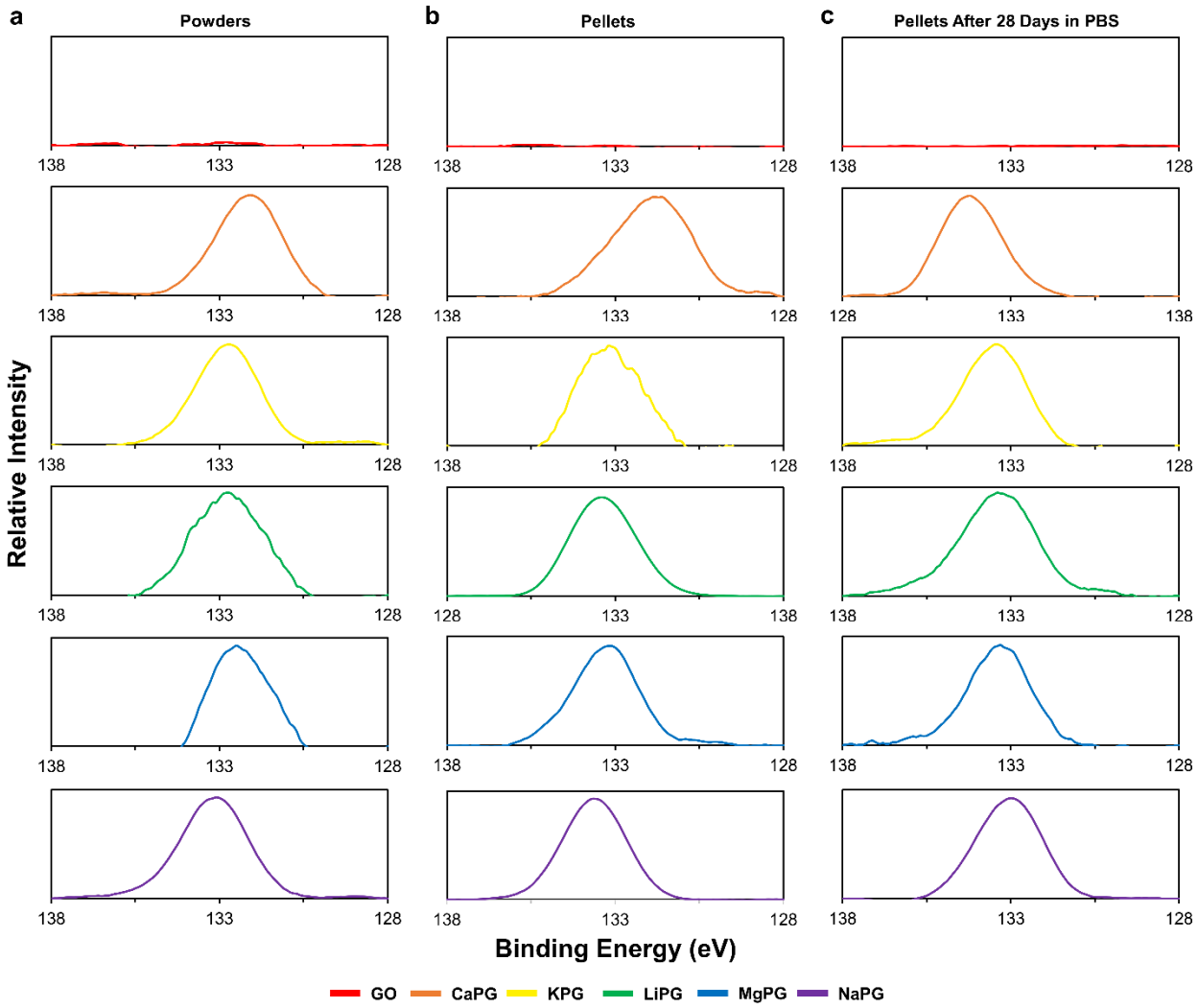

Fig. S6. P2p spectra from high resolution XPS of PG materials. P2p spectra of (*A*) powders, (*B*), pellets, and (*C*) pellets after 28 days in PBS at 37 °C. All processing was carried out as described in the methods.

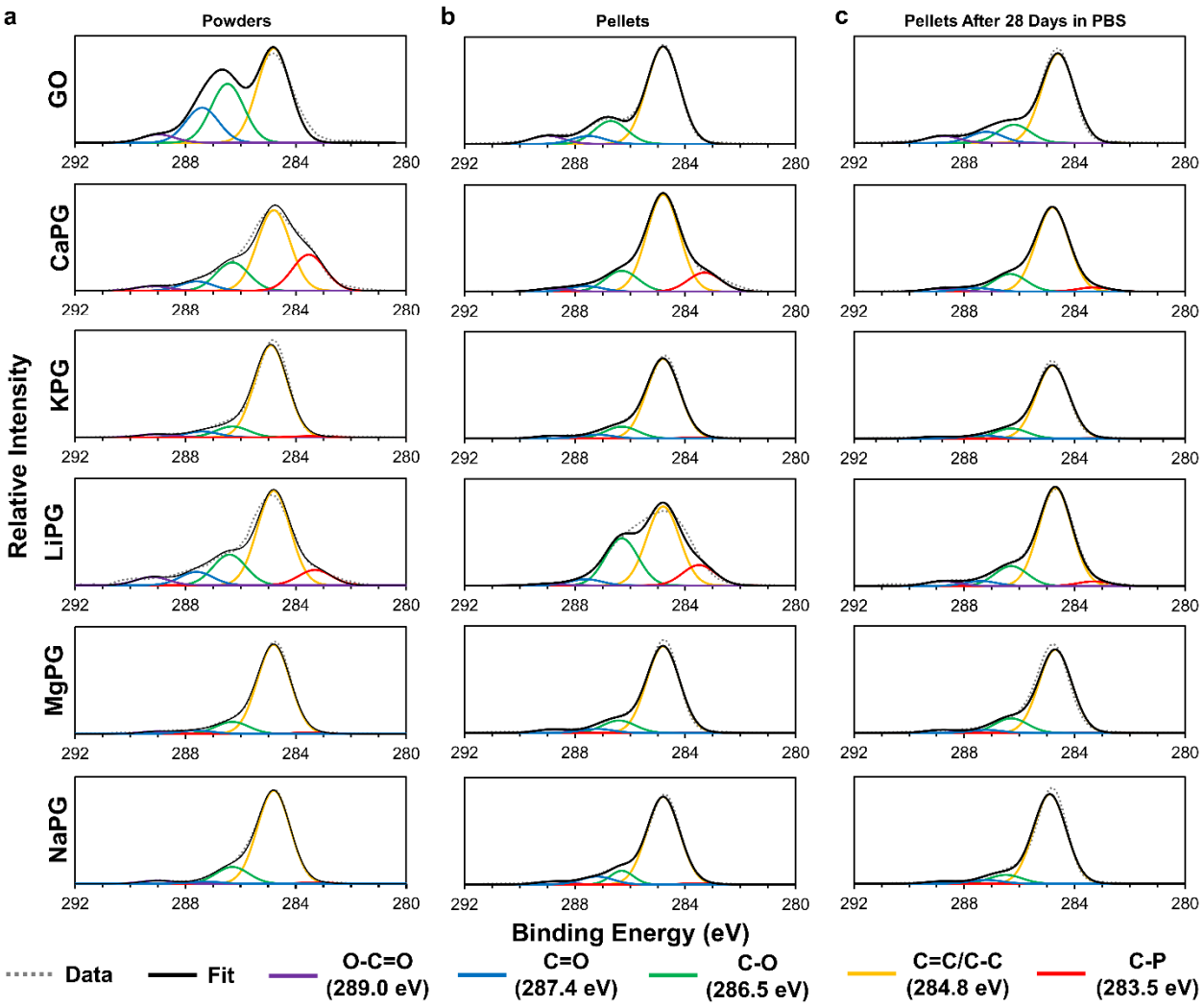

Fig. S7. Deconvoluted C1s spectra from high resolution XPS of PG materials. C1s spectra of (*A*) powders, (*B*) pellets, and (*C*) pellets after 28 days in PBS at 37 °C. All deconvolution was carried out as described in the methods. Peaks at 289.0 eV, 287.4 eV, 286.5 eV, 284.8 eV, and 283.5 eV that correspond to O–C=O (purple), C=O (blue), C–O (green), C=C/C–C (orange), and C–P (red) groups, respectively, are displayed.

Table S1. Atomic percentages of carbon functionalities. Data is quantified from the deconvolution of the C1s XPS peaks.

	Area Under the Curve (%)	GO	CaPG	KPG	LiPG	MgPG	NaPG
Powders	O-C=O (289.0 eV)	4.2	2.9	2.7	5.1	2.4	2.8
	C=O (287.4 eV)	17.8	5.8	5.1	8.2	3.1	2.0
	C-O (286.5 eV)	30.0	17.8	9.6	18.9	11.1	14.5
	C=C/C-C (284.8 eV)	48.1	50.7	81.6	58.2	82.2	79.8
	C-P (283.5 eV)	0.0	22.7	1.1	9.5	1.2	1.0
Pellets	O-C=O (289.0 eV)	6.1	2.1	2.8	1.1	3.4	2.8
	C=O (287.4 eV)	5.9	3.8	3.9	4.1	3.7	7.2
	C-O (286.5 eV)	16.8	14.3	11.9	30.5	11.6	8.9
	C=C/C-C (284.8 eV)	71.2	66.7	80.4	51.0	80.9	80.0
	C-P (283.5 eV)	0.0	13.1	1.1	13.2	0.4	1.1
Pellets After 28 Days in PBS	O-C=O (289.0 eV)	5.7	2.9	2.2	3.7	3.0	2.3
	C=O (287.4 eV)	9.0	3.3	3.4	3.7	2.9	3.5
	C-O (286.5 eV)	14.6	15.6	11.3	15.0	14.0	8.4
	C=C/C-C (284.8 eV)	70.7	74.4	82.6	74.0	79.9	85.3
	C-P (283.5 eV)	0.0	3.8	0.6	3.5	0.2	0.4

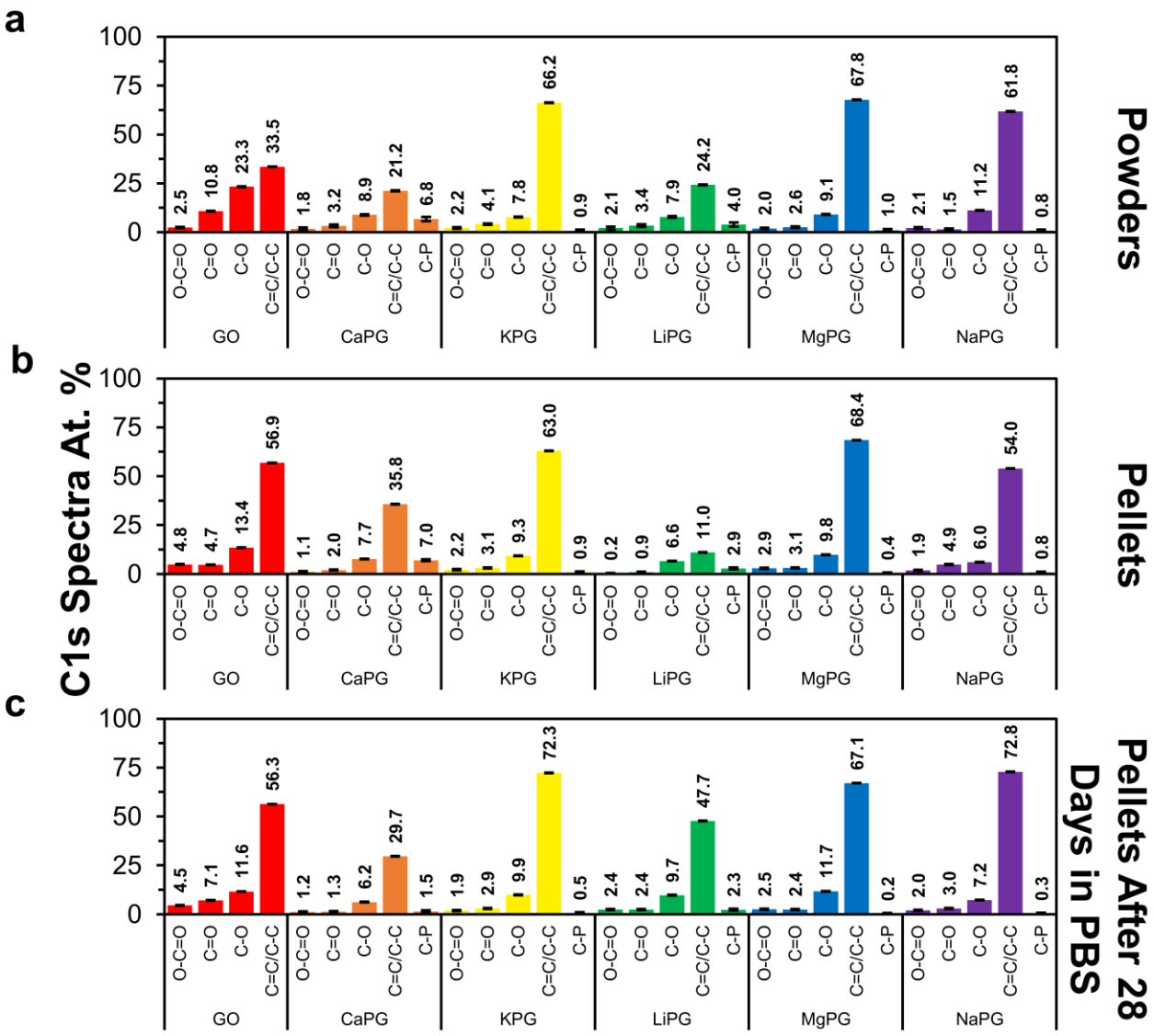

Fig. S8. Atomic percentages from XPS C1s spectra for PG materials. (*A*) Powders, (*B*) pellets, and (*C*) pellets after 28 days in PBS at 37 °C. Quantification was processed by normalizing the area of each peak (in At. % from Table S1) to the carbon composition from survey scans (Fig. S4). Error bars for GO represent a standard deviation for the peak fit constraints (described in the method) for each peak in the C1s spectra from GO powders (n = 3, where each scan was collected at a different spot on the sample). The remaining error bars represent a relative standard deviation for the peak fit constraints for each peak in the C1s spectra from CaPG powders (n = 3, where each scan was collected at a different spot on the sample).

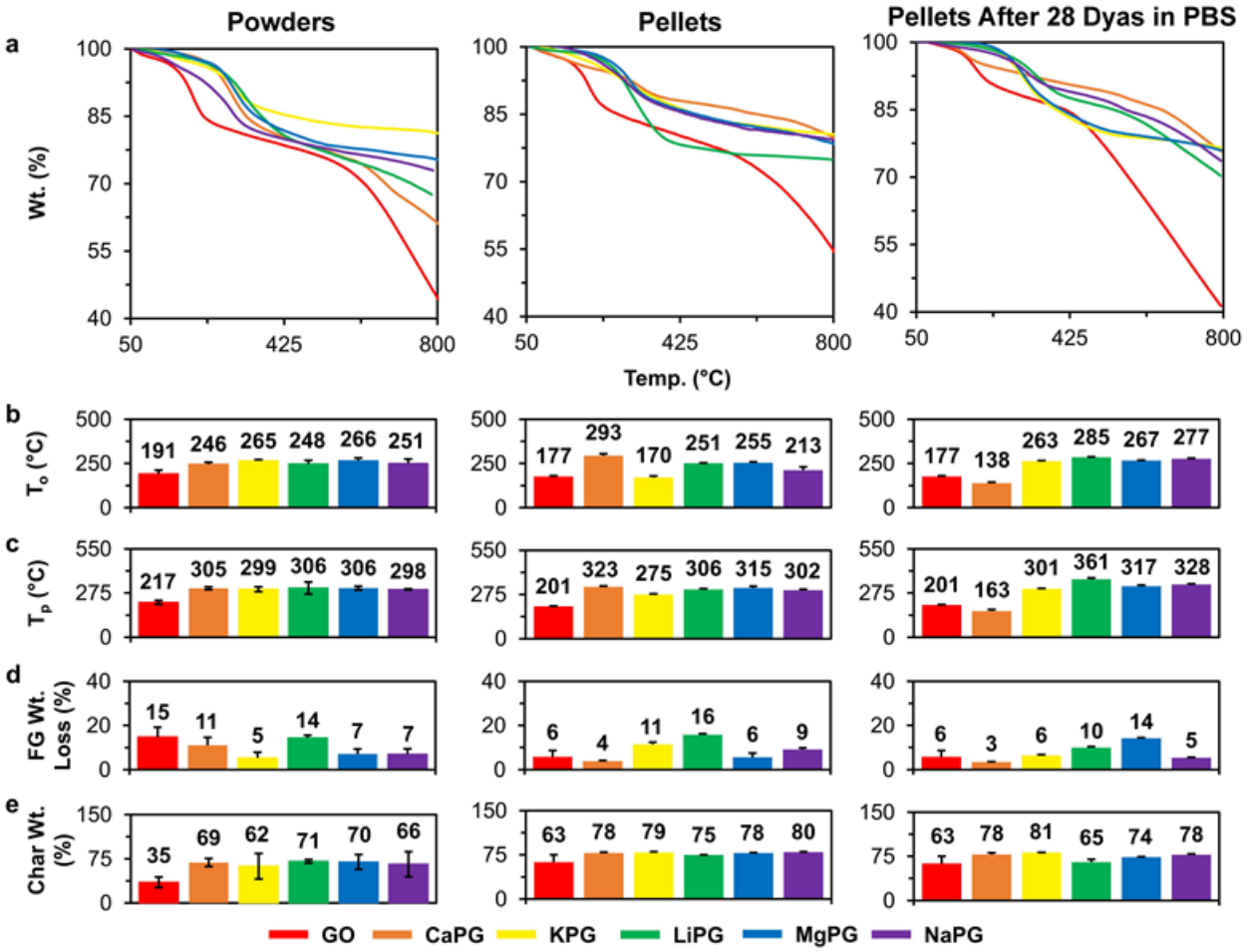

Fig. S9. TGA of PG powders, pellets, and pellets after 28 days in PBS at 37 °C. (*A*) Overlay of TGA thermograms. (*B*) Onset temperature (T_o) of the degradation event. (*C*) First derivative peak temperature (T_p). (*D*) Functional group weight loss (FG Wt. Loss). (*E*) Char weight (Char Wt.), which is the weight percent remaining at 800 °C. The bars and numerical values represent the mean of $n = 3$ samples and error bars are the standard deviation.

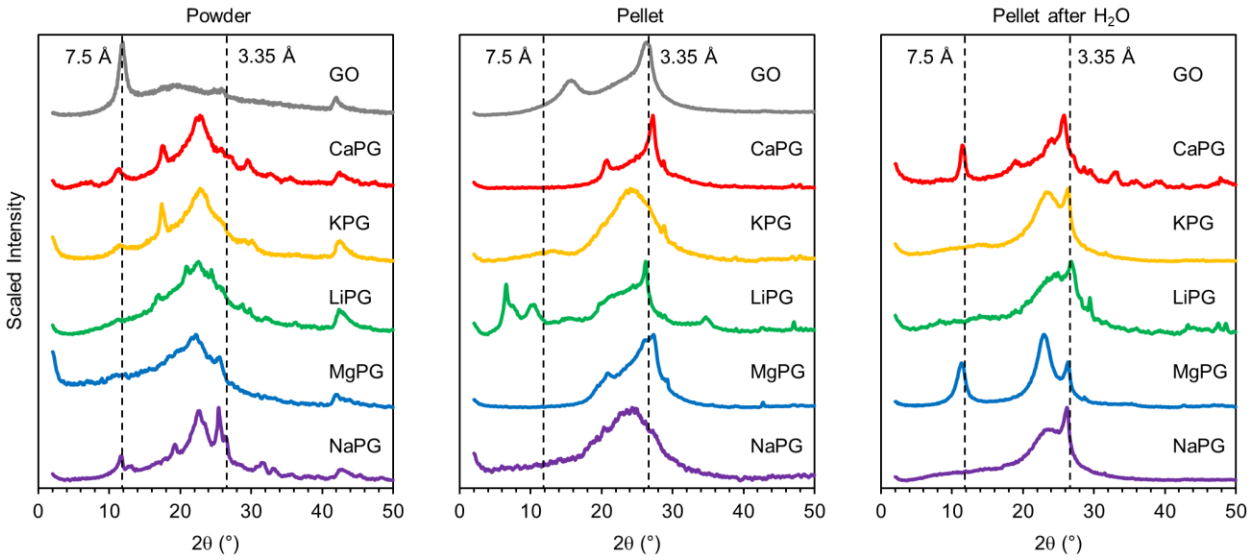

Fig. S10. XRD of PG materials. The dashed reference line at 26.6° (d_{hkl} = 3.35 Å) corresponds to the intergallery spacing for graphite, and the dashed reference line at 11.8° (d_{hkl} = 7.5 Å) corresponds to the intergallery spacing for graphene oxide.

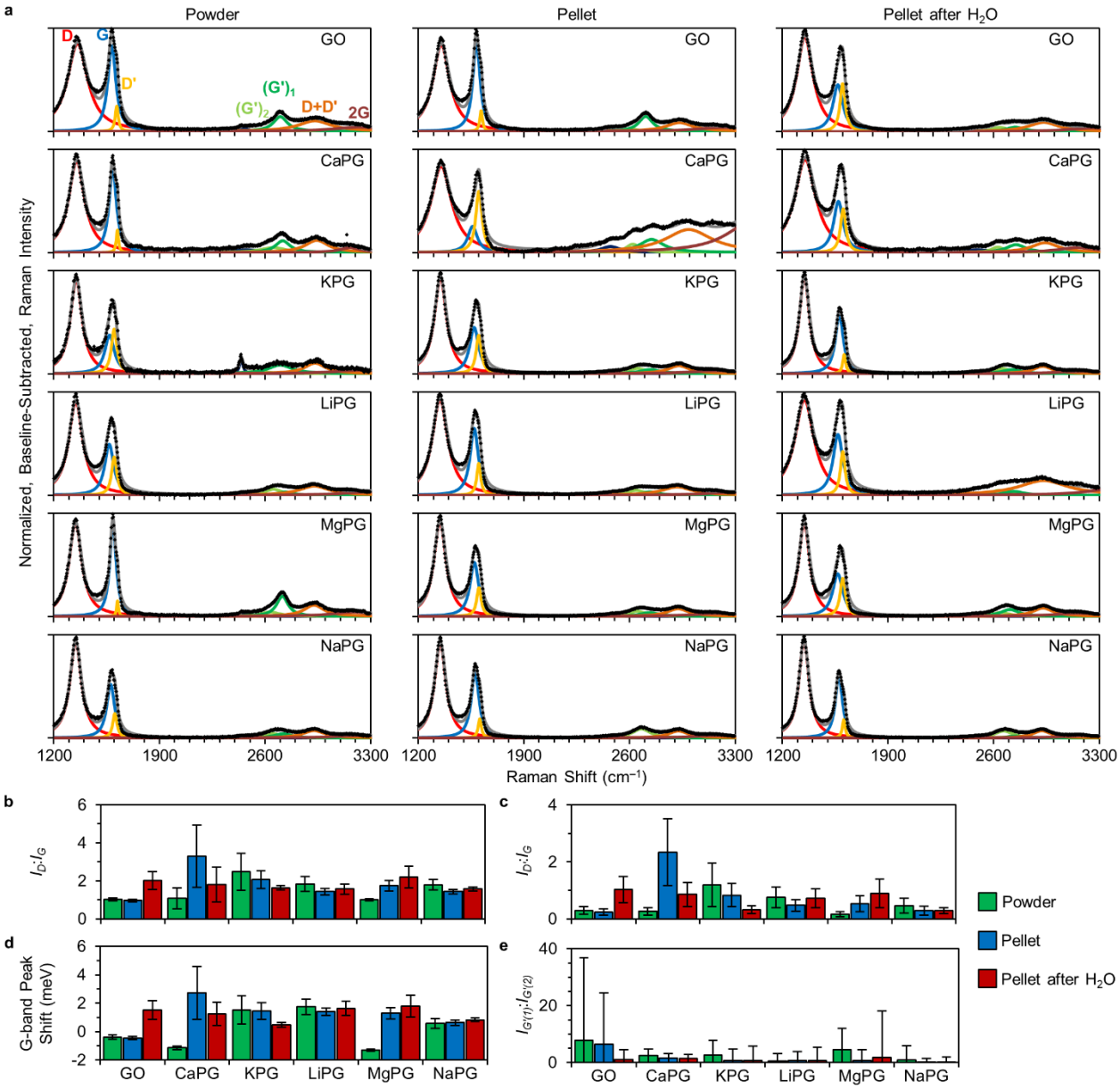

Fig. S11. Raman spectroscopy of PG materials. (*A*) Raman spectra (the black dots are the as acquired spectra, the gray line is the sum of all the fits, and the color lines are the fits to the indicated peaks). Quantification of (*B*) the ratio of the intensity of the D–band (I_D) to the intensity of the G–band (I_G), (*C*) the ratio of the intensity of the D'–band ($I_{D'}$) to the intensity of the G–band, (*D*) peak shift of the G–band compared to graphite, and (*E*) the ratio of the intensity of the $(G')_1$–band ($I_{G'(1)}$) to the intensity of the $(G')_2$–band ($I_{G'(2)}$).

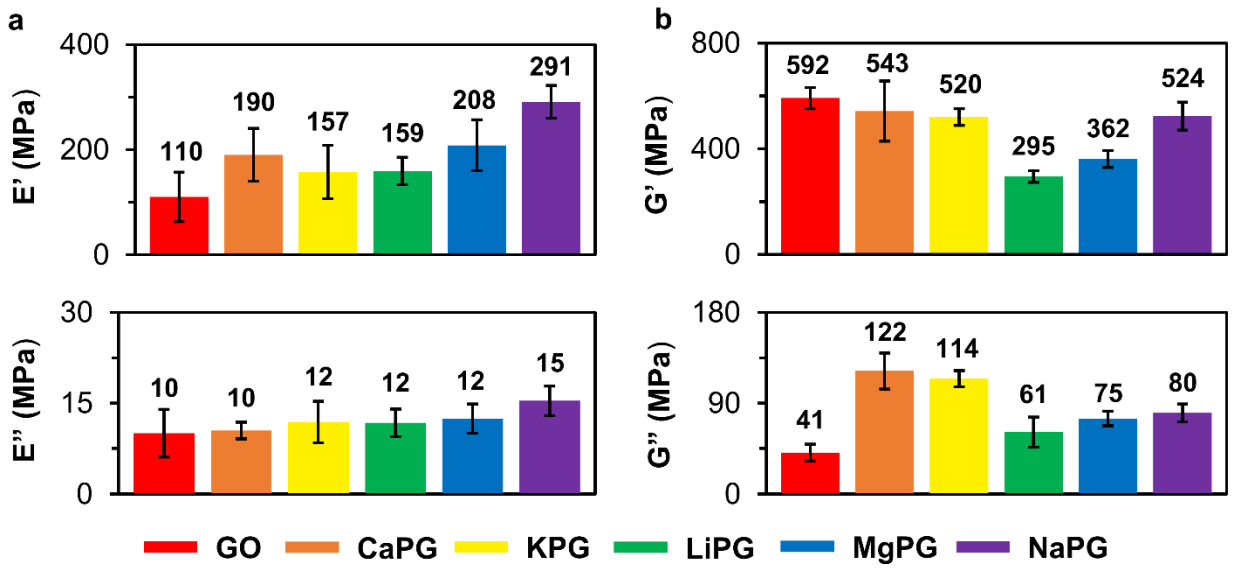

Fig. S12. Compressive mechanical properties of PG constructs. (*A*) Compressive DMA with storage moduli (*E'*) and loss moduli (*E''*) and (*B*) viscoelastic torsional shear testing, with storage moduli (*G'*) and loss moduli (*G''*) of pellets. Bars and numerical values are the mean for $n \geq 6$ pellets for all materials and the error bars are the standard deviation.

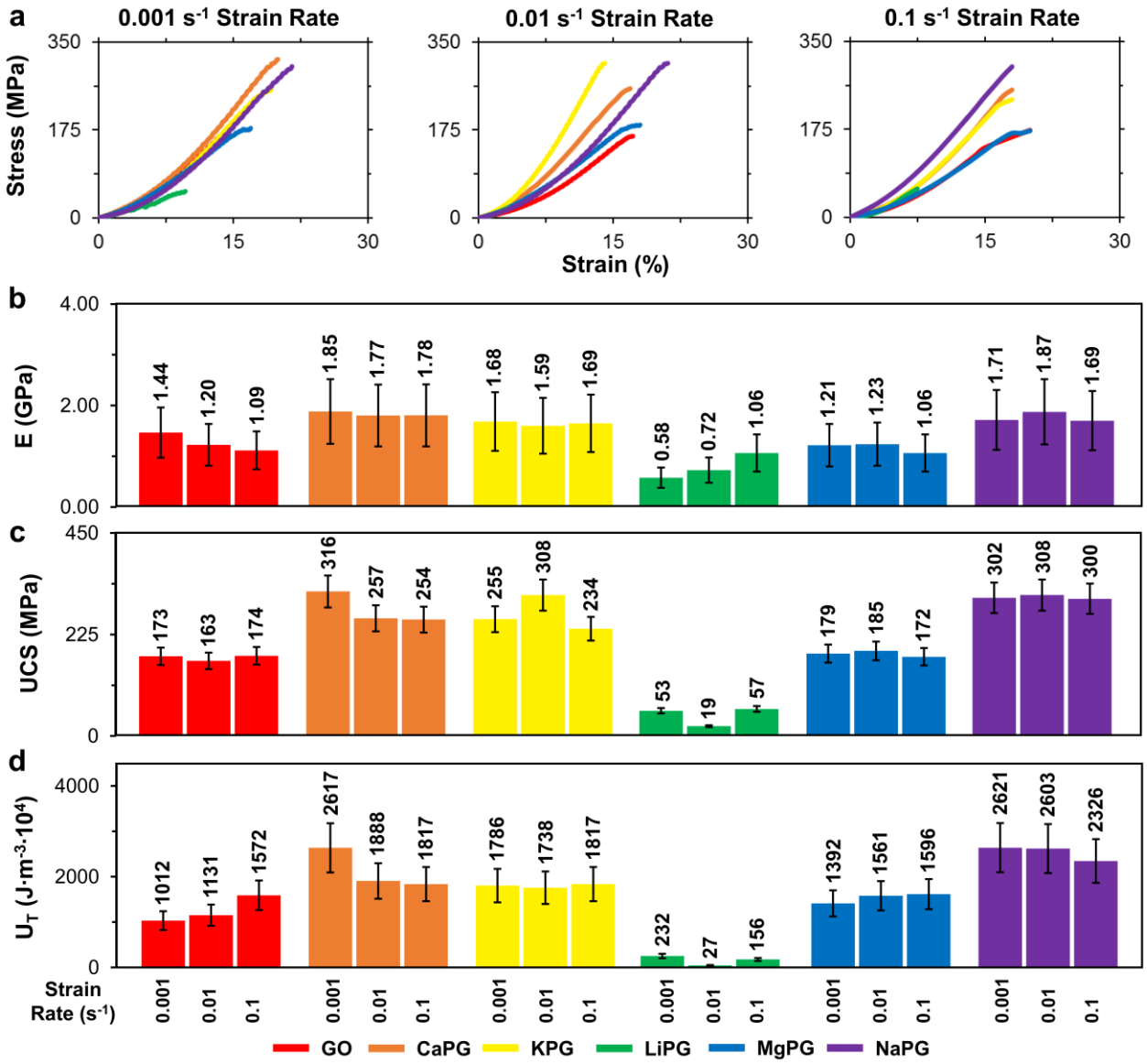

Fig. S13. Compressive universal testing of PG constructs at different strain rates. (*A*) Stress–strain curves. (*B*) Young's modulus (*E*). (*C*) Ultimate compressive strength (*UCS*). (*D*) Toughness (U_T). Note that error bars for *E*, *UCS*, and U_T are the relative standard deviation of GO pellets (n = 3) measured at a strain rate of 0.1 s^{-1}.

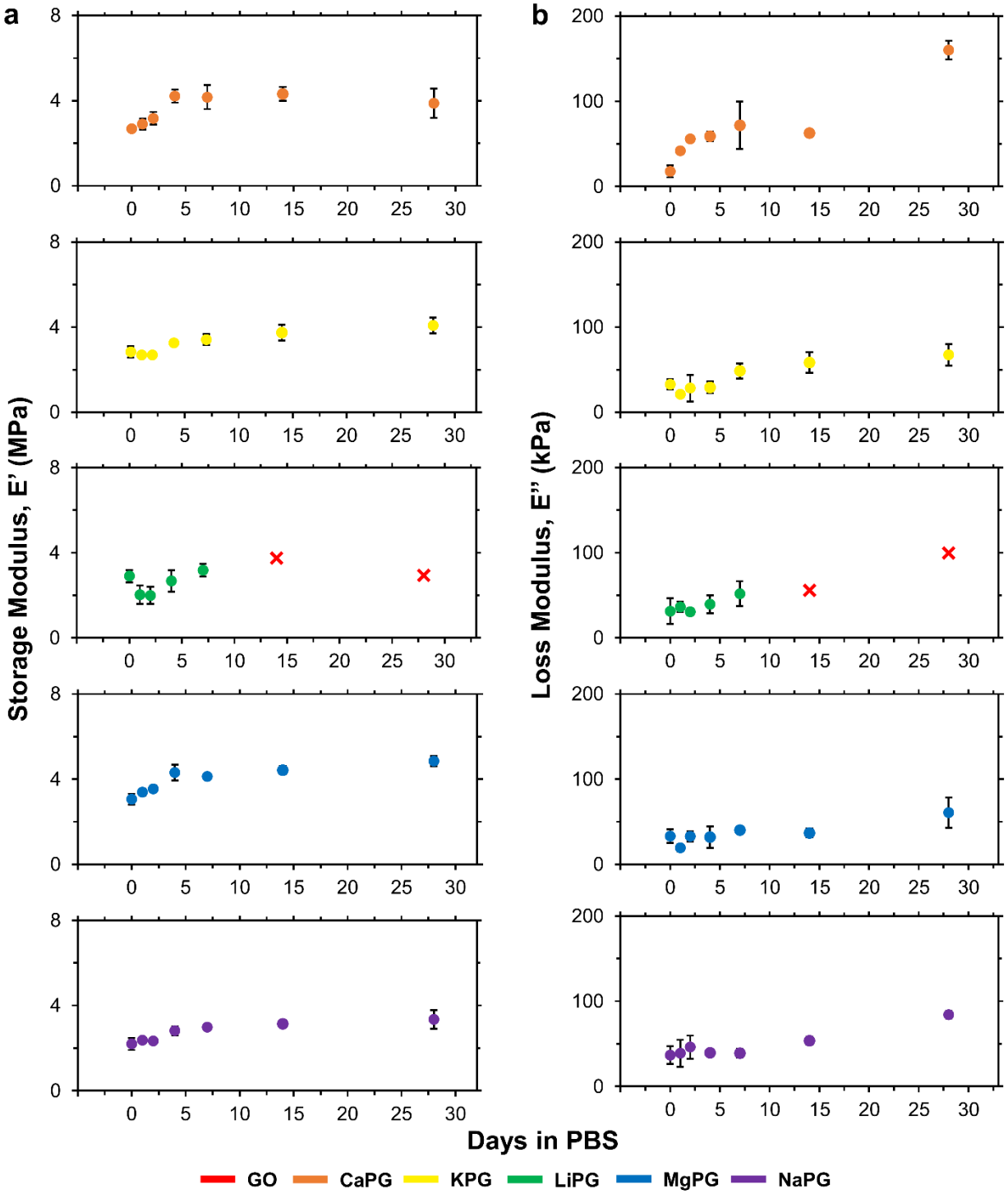

Fig. S14. Compressive DMA of PG constructs in PBS at 37 °C. (*A*) Storage moduli (*E'*) and (*B*) loss moduli (*E''*) of PG pellets as a function of time. The error bars represent the standard deviation between three different pellets for each material and × denotes mechanical failure. Note that GO is not reported due to the poor water stability of GO pellets.

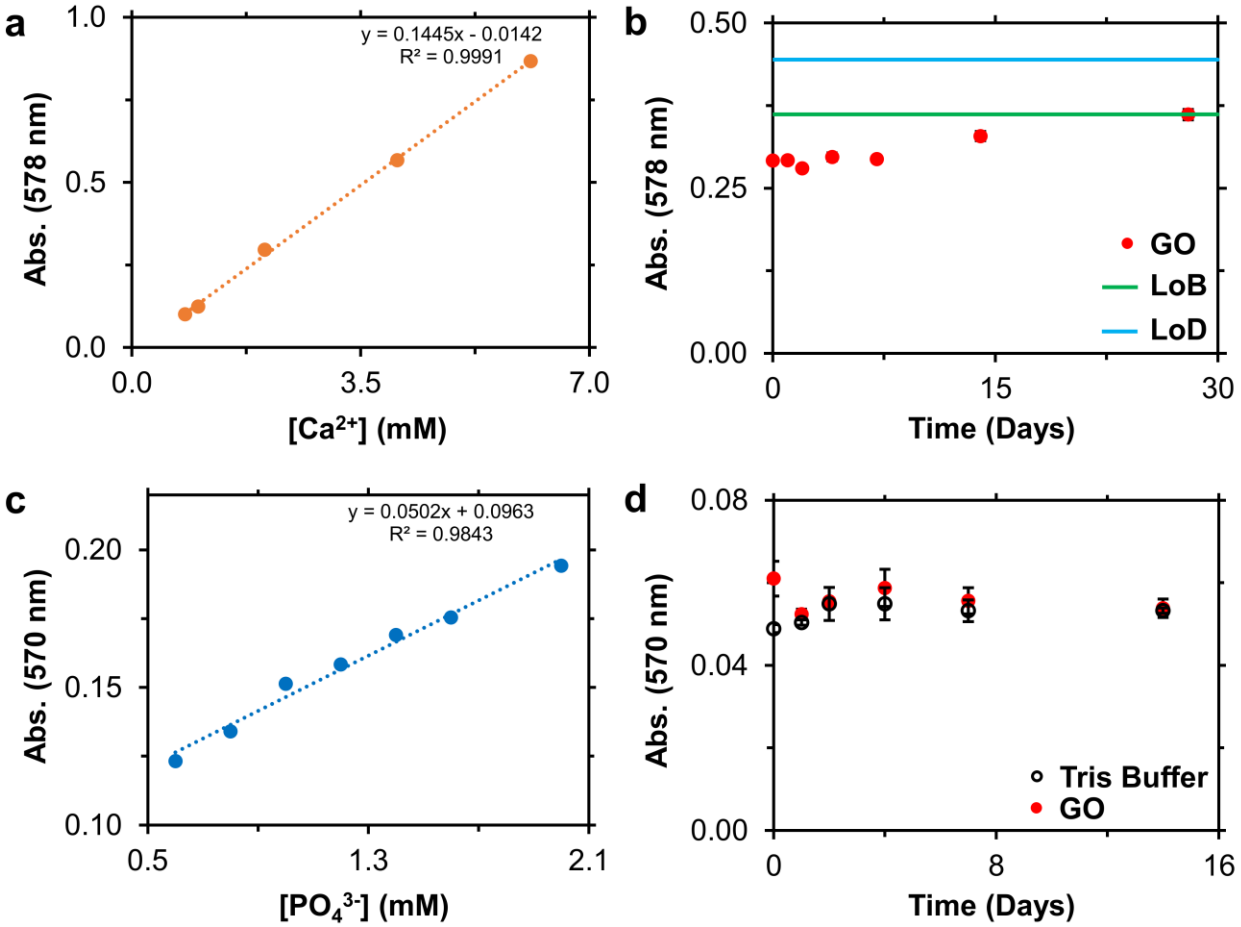

Fig. S15. Linear range of the *o*–cresolphthalein complexone assay and PiPer™ Phosphate Assay. (*A*) Calcium calibration curve. (*B*) Limit of Blank (LoB), Limit of Detection (LoD), and supernatants of GO pellets. (*C*) Phosphate calibration curve. (*D*) Absorbance of Tris buffer and supernatants of GO pellets. In panels (*A–B*), data was acquired using the *o*–cresolphthalein complexone assay. Panel (*A*) absorbances are background subtracted from a PBS blank and panel (*B*) is raw absorbance data. Further, the PiPer™ Phosphate Assay was used to acquire data in panels (*C-D*). Panel (*C*) absorbances are background subtracted from a Tris buffer blank while panel (*D*) is raw absorbance values. Note that for the *o*–cresolphthalein complexone assay and PiPer™ Phosphate Assay, supernatants from GO pellets (n = 3 for both assays) were run as additional negative controls to ensure trace graphenic materials did not interfere with the assays.

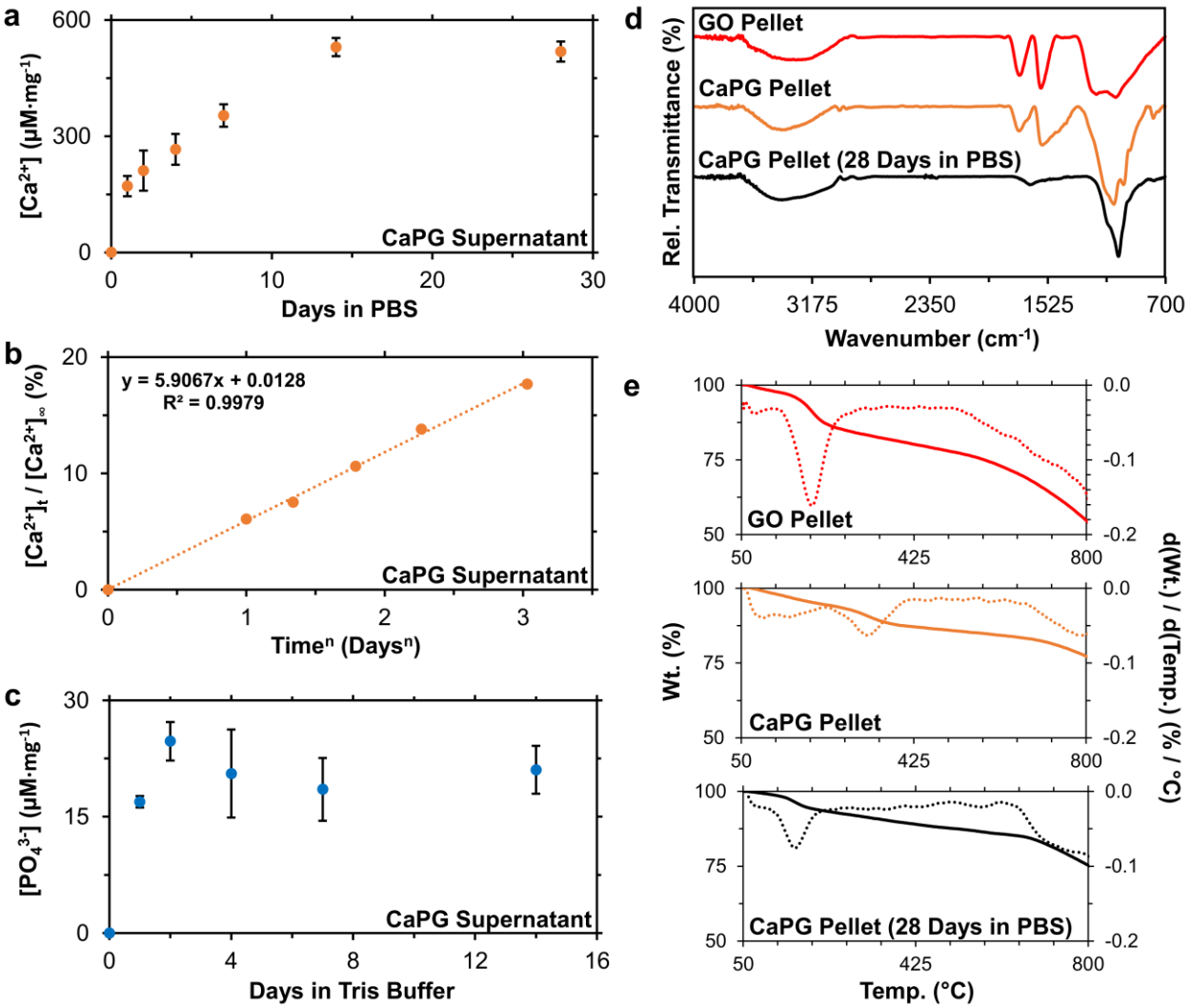

Fig. S16. Calcium and phosphate elution from CaPG and characterization of CaPG constructs after 28 days in PBS at 37 °C. (*A*) Calcium elution from CaPG over 28 days. (*B*) Calcium elution from CaPG fit to Korsmeyer–Peppas model (n = 0.42). (*C*) Phosphate elution from CaPG over 14 days. (*D*) FTIR spectra. (*E*) TGA thermograms (solid lines) and first derivative of thermograms (dashed lines). In panels (*A*–*B*), data was acquired using the *o*–cresolphthalein complexone assay while panel (C) was acquired using the PiPer™ Phosphate Assay. The error bars in panels (*A*) and (*C*) represent the standard deviation of three separate pellets for each time point. Lastly, data from panels (*D*–*E*) was obtained after CaPG constructs were exposed to PBS at 37 °C for 28 days.

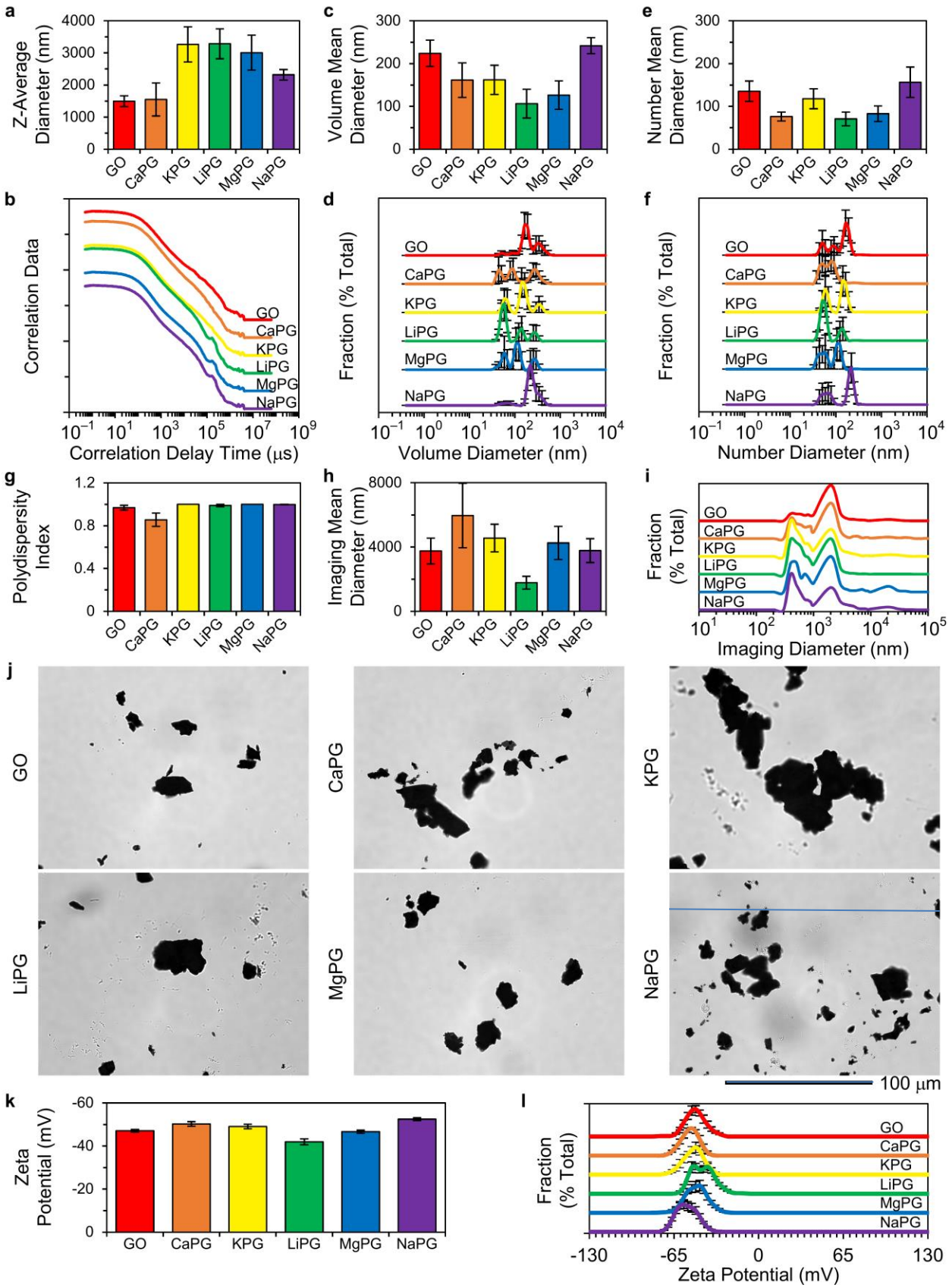
a
Z-Average Diameter (nm)
4000
3000
2000
1000
0
GO
CaPG
KPG
LiPG
MgPG
NaPG
c
Volume Mean Diameter (nm)
300
200
100
0
e
Number Mean Diameter (nm)
b
Correlation Data
Correlation Delay Time (μs)
d
Fraction (% Total)
Volume Diameter (nm)
f
Number Diameter (nm)
g
Polydispersity Index
1.2
0.8
0.4
h
Imaging Mean Diameter (nm)
8000
4000
i
Imaging Diameter (nm)
j
k
Zeta Potential (mV)
-60
-40
-20
l
-130
-65
0
65
130
100 μm

Fig. S17. Particle characterization. (*A*) Z–Average diameter (also known as the Cumulants mean or scattered light intensity-weighted harmonic mean particle diameter) determined by dynamic light scattering (DLS) and Cumulants analysis. Bars are sample mean and error bars are standard error for the as-determined Z-Average diameter from 5 measurements. (*B*) Average autocorrelation plots from DLS. Data are offset for clarity. (*C*) Volume mean particle diameter, calculated by Zetasizer Software from the intensity data of A and B. (*D*) The average distribution of the volume-based diameter from 5 measurements. Error bars are standard error. Data are offset for clarity. (*E*) Number mean particle diameter, calculated by Zetasizer Software from the intensity data of A and B. (*F*) The average distribution of the number-based diameter from 5 measurements. Error bars are standard error. Data are offset for clarity. Note that the volume and number data are calculated using assumptions that are not fulfilled by real data; thus, these results are for comparative purposes and are not accurate representations of reality. (*G*) Average polydispersity index of the Cumulants fit of the autocorrelation data of B. The values are extremely high (~1), indicating a very polydisperse sample. When polydispersity is this high, DLS measurements are not accurate. Error bars are standard error. (*H*) Image mean particle diameter determined *via* high-resolution optical microscopy. Bars are sample mean and error bars are standard error. At least 400 particles were quantified for each sample. (*I*) The distribution of image-determined particle diameters. Data are offset for clarity. (*J*) Representative optical images of aqueous suspensions of GO and PGs that were drop cast onto microscope slides. (*K*) Mean Zeta potential of graphenic materials dispersed in DI water at 100 $\mu g\ mL^{-1}$ from 5 measurements. Bars are sample mean and error bars are standard error. (*L*) Average Zeta potential distributions from 5 measurements. Error bars are standard error. Data are offset for clarity.

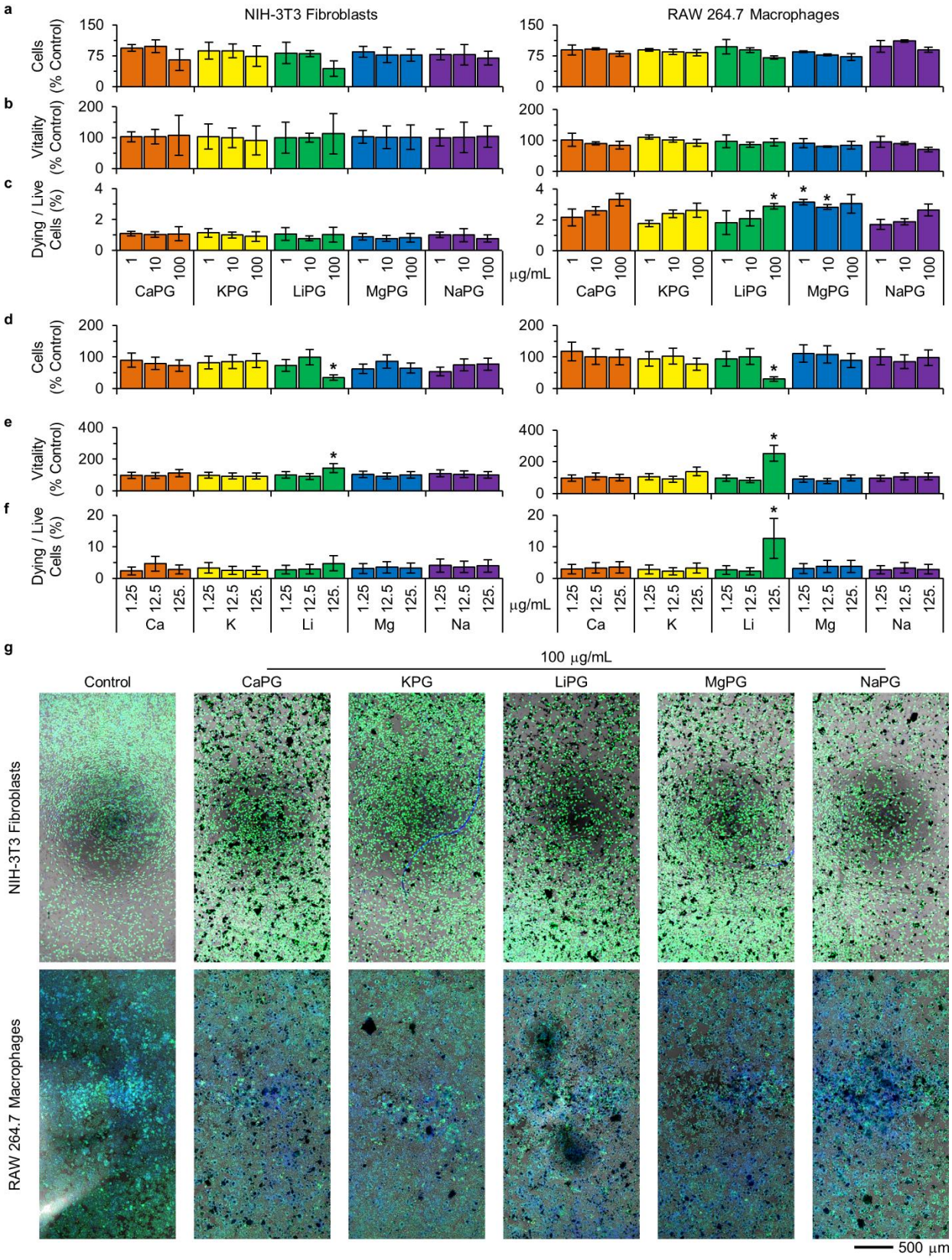

Fig. S18. Cytocompatibility of PG materials. (*A*) Cell enumeration assessed *via* Hoechst 33342–labeled nuclei, (*B*) cellular vitality assessed *via* Calcein AM, and (*C*) and late apoptotic and

necrotic cells assessed *via* ethidium homodimer–1 as a percent of all cells for NIH–3T3 fibroblasts and RAW 264.7 macrophages exposed to varying concentrations of PG materials. (*D–F*) Cytocompatibility assays for cells exposed to high concentrations of counter ions. All anions were chloride. Since XPS showed that the cations are on the order of 10 wt.% of the PG materials, the corresponding PG concentrations would approximately be 12.5, 125, and 1250 mg mL^{-1}, without accounting for the slow, controlled release of the cations from the PG materials over time. (*G*) Representative overlay images of concatenated fields of view of Hoechst 33342 (blue), Calcein AM (green), and ethidium homodimer–1 (red) fluorescence and phase contrast (gray). Note that the error bars are sample standard deviation, and * indicates a statistically significant difference compared to control.

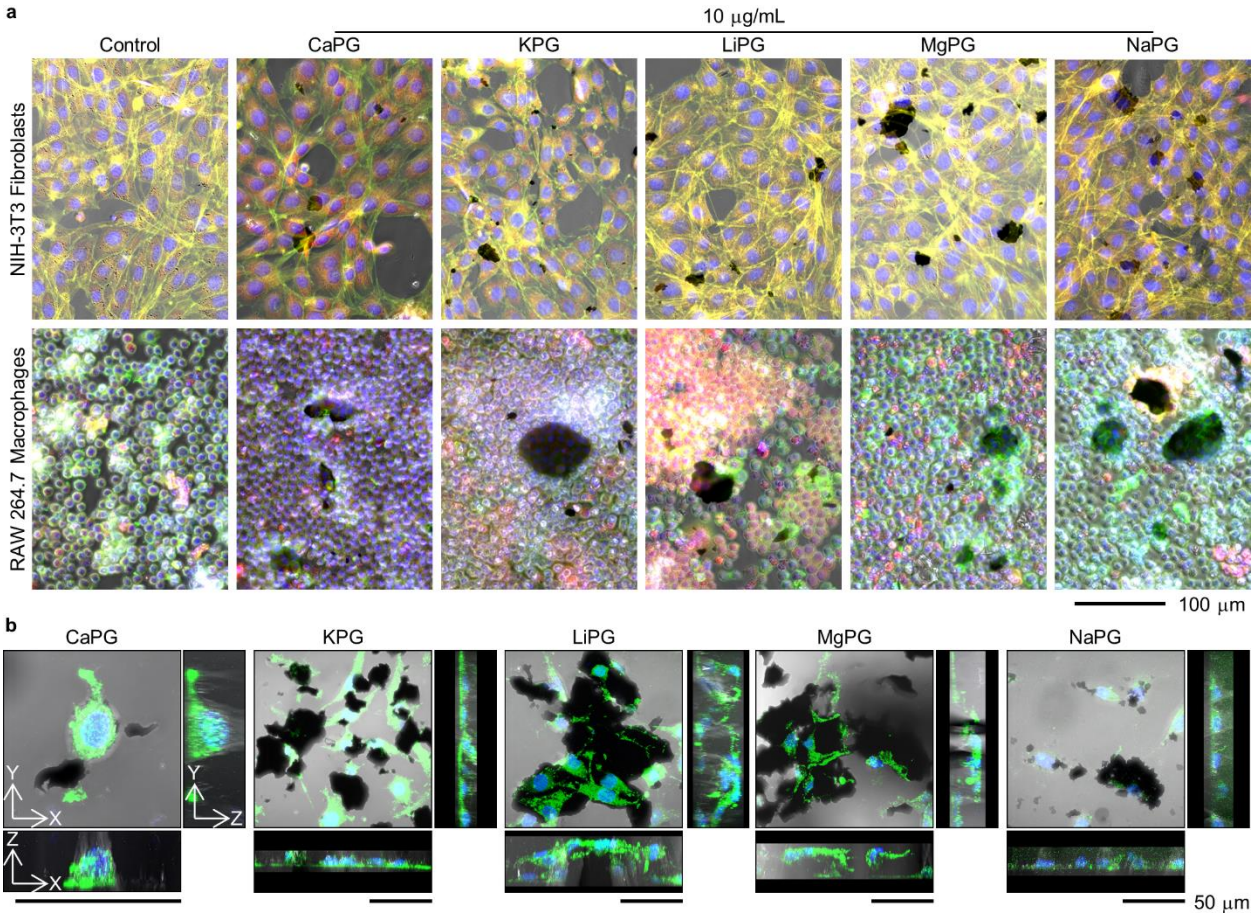

Fig. S19. Sub–cellular imaging of cellular interactions with PG materials. (*A*) Overlay images of fluorescently labeled, sub–cellular compartments. Blue is Hoechst 33342 that labels nuclei; green is Acti–stain^{TM} 488 phalloidin that labels filamentous actin; red is MitoTracker® that labels mitochondria; and grayscale is phase contrast. The dark regions are likely PG materials. Cells were exposed to 10 μg mL^{-1} for 24 h. (*B*) Confocal maximum projections of Z–stacks of NIH–3T3 fibroblasts grown on PG substrates. Blue represents Hoechst 33342 fluorescence from the nuclei; green represents Calcein AM fluorescence within cytoplasm; and grayscale represents cellular and PG material features. Overall, PG materials did not alter these sub–cellular compartments, and fibroblasts could adhere to and grown on PG material substrates.

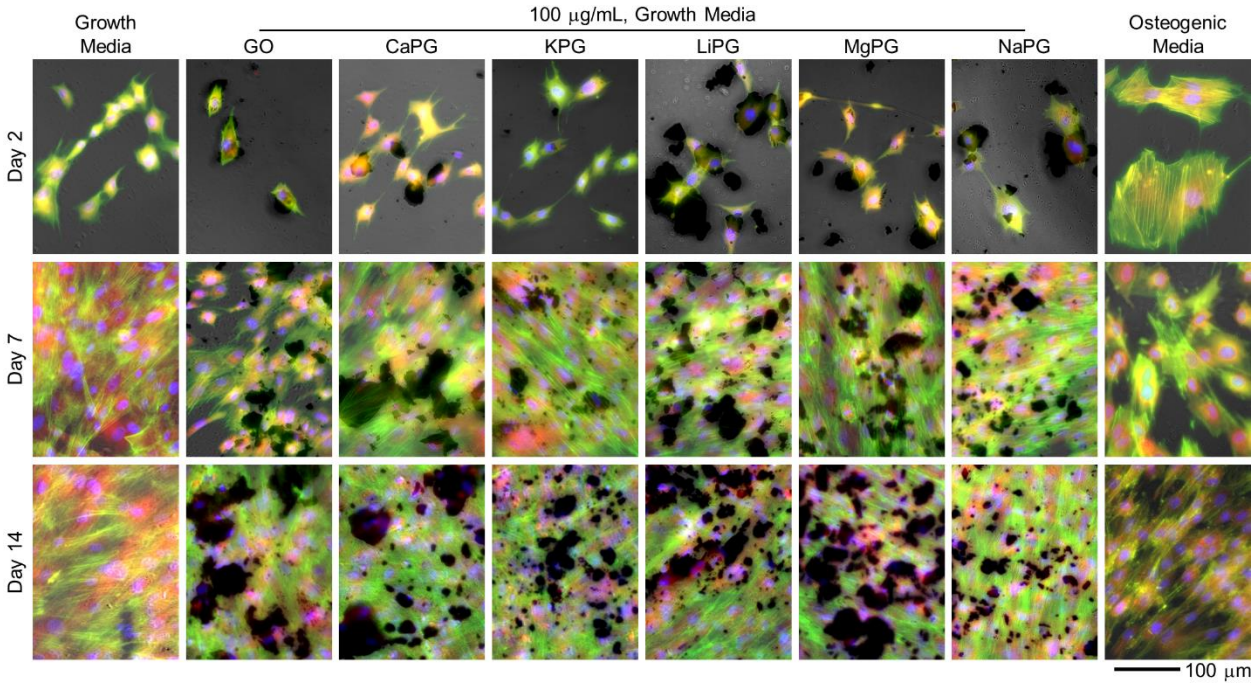

Fig. S20. Imaging of sub–cellular compartments of hMSCs exposed to PG materials for varying time. Blue is Hoechst 33342 that labels nuclei; green is Acti–stain^{TM} 488 phalloidin that labels filamentous actin; red is MitoTracker® that labels mitochondria; and grayscale is phase contrast. Exposure of hMCSs to high concentrations of PG materials did not alter these sub–cellular compartments.

Fig. S21. Images of the *in vivo* procedure. Mice were anesthetized through a nose cone under isoflurane, shaven, and cleaned with 70% ethanol. A dose of 0.54 mg (approximately 20 mg kg^{-1}) in 50 μL of PBS was injected subcutaneously on either side of the dorsum, using a 27 gauge insulin syringe. The NSG/Col3.6Topaz mice received 1×10^6 BMSCs per injection site, mixed with the material prior to injection. The (GO+rhBMP–2) and (GO+rhBMP–2+BMSCs) study groups received 2.5 μg of rhBMP–2, mixed with GO prior to injection, per injection site.

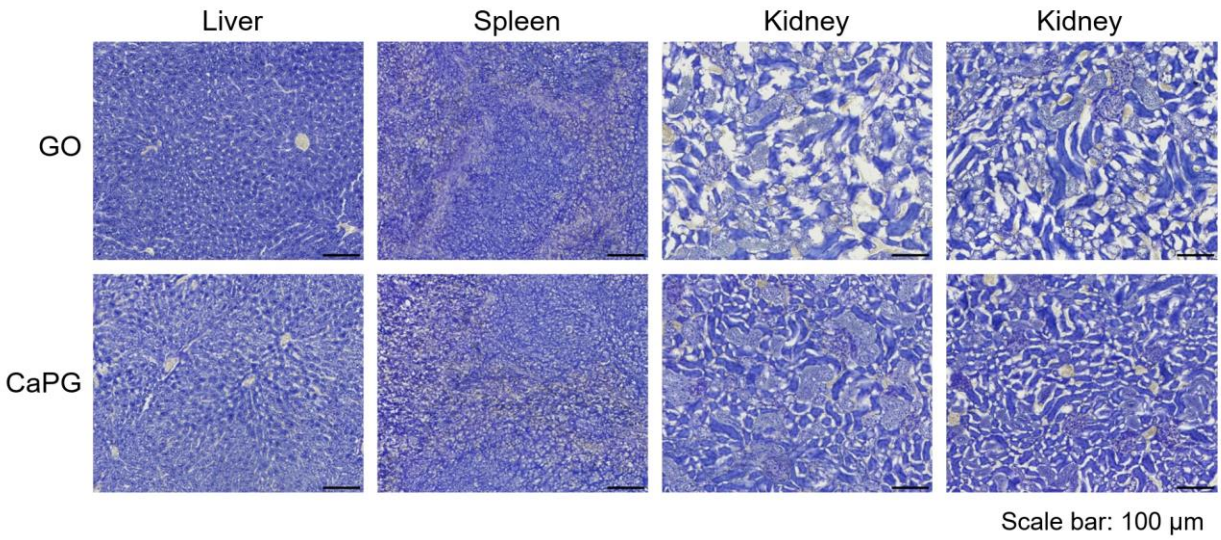

Fig. S22. Histological images of major clearance organs after 8 weeks. The liver, spleen, and kidneys of mice injected with GO and CaPG (without cells) were harvested, sectioned and stained with toluidine blue. There was no accumulation of material or obvious tissue damage.

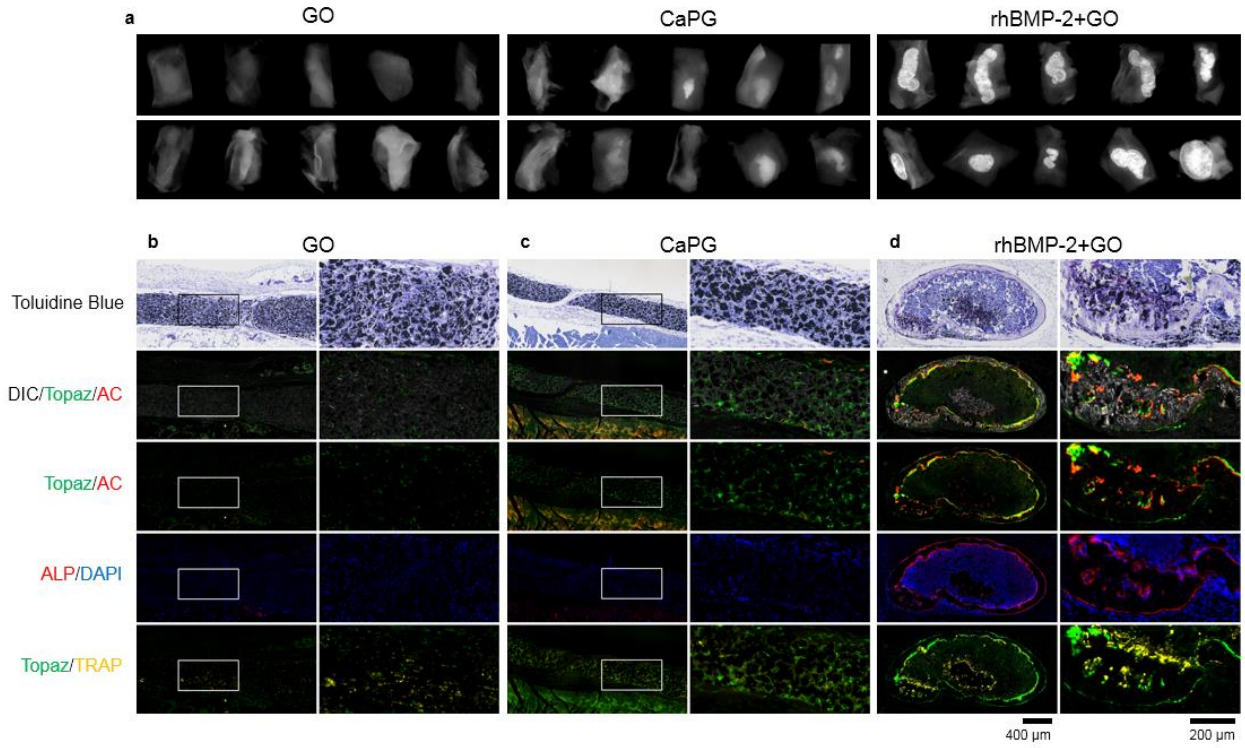

Fig. S23. X–ray and histological images of samples with no cells after 8 weeks. (*A*) Representative X–ray images of the harvested subcutaneous tissue. (*B–D*) Histology showing toluidine blue and overlay images of darkfield (DIC), donor cells (cyan), host (topaz), alizarin complexone (AC, red), alkaline phosphatase (ALP, red), DAPI (blue), and TRAP (yellow). Host–derived fibroblasts are expressing faint topaz signals and are negative for AC, ALP or TRAP. The yellow cells in (*B*) identified by their faint TRAP staining are most likely macrophages.

Supplementary References:

1. Hummers WS, Offeman RE (1958) Preparation of Graphitic Oxide. *J Am Chem Soc* 80(6):1339–1339.

2. Holt BD, Arnold AM, Sydlik SA (2016) In It for the Long Haul: The Cytocompatibility of Aged Graphene Oxide and Its Degradation Products. *Advanced Healthcare Materials* 5(23):3056–3066.

3. Goods JB, Sydlik SA, Walish JJ, Swager TM (2014) Phosphate Functionalized Graphene with Tunable Mechanical Properties. *Advanced Materials* 26(5):718–723.

4. ASTM Committee D-20 on Plastics (2008) *Standard test method for compressive properties of rigid plastics* (ASTM International).

5. Calcium O-CPC (2011) Available at: http://www.spectrum-diagnostics.com/new/pdf/01_Clinical_Chemistry/03_Electrolytes/Calcium%20O-CPC.pdf [Accessed December 21, 2016].

6. Armbruster DA, Pry T (2008) Limit of Blank, Limit of Detection and Limit of Quantitation. *Clin Biochem Rev* 29(Suppl 1):S49–S52.

7. Dash S, Murthy PN, Nath L, Chowdhury P (2010) Kinetic modeling on drug release from controlled drug delivery systems. *Acta Pol Pharm* 67(3):217–223.

8. Lysdahl H, Baatrup A, Nielsen AB, Foldager CB, Bünger C (2013) Phenol Red Inhibits Chondrogenic Differentiation and Affects Osteogenic Differentiation of Human Mesenchymal Stem Cells in Vitro. *Stem Cell Reviews and Reports* 9(2):132–139.

9. Livak KJ, Schmittgen TD (2001) Analysis of Relative Gene Expression Data Using Real-Time Quantitative PCR and the $2^{-\Delta\Delta CT}$ Method. *Methods* 25(4):402–408.

10. Dyment NA, et al. (2015) Gdf5 progenitors give rise to fibrocartilage cells that mineralize via hedgehog signaling to form the zonal enthesis. *Dev Biol* 405(1):96–107.

11. Jiang X, et al. (2005) Histological Analysis of GFP Expression in Murine Bone. *J Histochem Cytochem* 53(5):593–602.

12. Dyment NA, et al. (2016) High-Throughput, Multi-Image Cryohistology of Mineralized Tissues. *J Vis Exp* (115). doi:10.3791/54468.

13. Moore DS, McCabe GP, Craig BA (2014) *Introduction to the Practice of Statistics* (Macmillan Higher Education).

14. Sun J, et al. (2014) Formation of Stable Phosphorus–Carbon Bond for Enhanced Performance in Black Phosphorus Nanoparticle–Graphite Composite Battery Anodes. *Nano Lett* 14(8):4573–4580.

15. Liu Y, et al. (2017) Red Phosphorus Nanodots on Reduced Graphene Oxide as a Flexible and Ultra-Fast Anode for Sodium-Ion Batteries. *ACS Nano* 11(6):5530–5537.

16. Larkin P (2017) *Infrared and Raman Spectroscopy: Principles and Spectral Interpretation* (Elsevier).

17. Coates J (2006) Interpretation of Infrared Spectra, A Practical Approach. *Encyclopedia of Analytical Chemistry* (John Wiley & Sons, Ltd). doi:10.1002/9780470027318.a5606.

18. Sydlik SA, Jhunjhunwala S, Webber MJ, Anderson DG, Langer R (2015) In Vivo Compatibility of Graphene Oxide with Differing Oxidation States. *ACS Nano* 9(4):3866–3874.

19. Ionita M, et al. (2017) Graphene and functionalized graphene: Extraordinary prospects for nanobiocomposite materials. *Composites Part B-Engineering* 121:34–57.

20. Dimiev AM, Alemany LB, Tour JM (2013) Graphene Oxide. Origin of Acidity, Its Instability in Water, and a New Dynamic Structural Model. *ACS Nano* 7(1):576–588.

21. Kurapati R, et al. (2015) Dispersibility-Dependent Biodegradation of Graphene Oxide by Myeloperoxidase. *Small* 11(32):3985–3994.

22. Kurapati R, et al. (2018) Covalent chemical functionalization enhances the biodegradation of graphene oxide. *2D Materials* 5(1):015020.

23. Sydlik SA, Jhunjhunwala S, Webber MJ, Anderson DG, Langer R (2015) *In Vivo* Compatibility of Graphene Oxide with Differing Oxidation States. *ACS Nano* 9(4):3866–3874.

24. Holt BD, Arnold AM, Sydlik SA (2017) Peptide-functionalized reduced graphene oxide as a bioactive mechanically robust tissue regeneration scaffold. *Polymer International* 66(8):1190–1198.

25. Liu J-H, et al. (2012) Effect of size and dose on the biodistribution of graphene oxide in mice. *Nanomedicine (Lond)* 7(12):1801–1812.

26. Ratner BD, Hoffman, Allan S., Schoen, Frederick J., Lemons, Jack E. eds. (2004) *Biomaterials Science: An Introduction to Materials in Medicine* (Academic Press, San Diego, California). 2nd Ed.

27. Holt BD, Wright ZM, Arnold AM, Sydlik SA (2016) Graphene oxide as a scaffold for bone regeneration: Graphene oxide for bone regeneration. *Wiley Interdisciplinary Reviews: Nanomedicine and Nanobiotechnology*. doi:10.1002/wnan.1437.

28. Pollard TD, Earnshaw WC, Lippincott-Schwartz J (2008) *Cell Biology* (Saunders/Elsevier).